Key Points:
- GPS data collected in South Iceland during 2001-2015 show significant temporal and spatial variation in station velocities
- The crustal deformation includes signals of plate spreading, postseismic transients, subsidence in Hengill, and uplift around Hekla volcano
- Strain rates estimated from GPS velocities show increased strain rates in the epicentral region prior to two *M*6 earthquakes in May 2008

Supporting Information:
- Supporting Information S1
- Data Set S1
- Data Set S2

Correspondence to:
T. Árnadóttir,
thora1@hi.is

A Preseismic Strain Anomaly Detected Before *M*6 Earthquakes in the South Iceland Seismic Zone From GPS Station Velocities

Thóra Árnadóttir[1] [ID], John Haines[2], Halldór Geirsson[1], and Sigrún Hreinsdóttir[3] [ID]

[1]Nordic Volcanological Center, Institute of Earth Sciences, University of Iceland, Reykjavík, Iceland, [2]GNS Science, Dunedin, New Zealand, [3]GNS Science, Lower Hutt, New Zealand

Abstract The South Iceland Seismic Zone (SISZ) accommodates E-W translation due to oblique spreading between the North American and the Eurasian plates in South Iceland with ruptures on N-S faults. Strain is released in earthquake sequences that last days to years, at average intervals of 80–100 years. Two *M*6.5 earthquakes struck in the SISZ in June 2000, and two *M*6 earthquakes in May 2008. These events released only half of the strain accumulated since the last earthquake sequence in 1896–1912. GPS station velocities are estimated from annual campaigns and continuous measurements in the SISZ during 2001–2015. The GPS station velocities are used to calculate strain rates from a new method using the vertical derivatives of horizontal stress. Our new strain rates are obtained by integrating vertical derivatives of horizontal stress rates, rather than differentiating interpolated GPS velocities, allowing finer resolution of strain. Estimating the strain rates for eight time intervals, we find high strain rates in the SISZ (0.5–1 microstrain per year) with significant temporal and spatial variation. The strain rates in the SISZ reveal contraction in the Hengill area and dilatation over a large area in eastern SISZ, indicating inflation of the magma system beneath Hekla volcano. A prominent strain anomaly is evident in the epicentral area prior to the May 2008 earthquakes. We suggest that this signal is primarily caused by plate motion and an increase in the rate of contraction in the Hengill area, located ∼10 km west of the epicentral area.

1. Introduction

Detecting geophysical signals before earthquakes has long been sought after within the Earth sciences. Iceland has been considered an ideal area for crustal deformation studies, since the initial idea of continental drift was put forth by Wegener in the late 1930s, with one of the first GPS measurement campaigns in the world conducted in Iceland in 1986. Observing crustal deformation signals related to earthquakes on the numerous N-S faults in the South Iceland Seismic Zone (SISZ) is one of the motivations for the dense GPS network reported here.

Iceland is spreading at a rate of about 18–19 mm/year due to relative plate motion of the North American and Eurasian plates in the North Atlantic (DeMets et al., 2010). The extension is accommodated by rifting and transform motion across the island. The most active seismic area in south Iceland is the SISZ, a transform zone that accommodates E-W left lateral shear at depth by right-lateral strike-slip faulting on a number of N-S oriented faults in the brittle crust (e.g., Árnadóttir et al., 2006; Einarsson et al., 2006). The SISZ transform zone is located between two active volcanic centers: Hengill to the west and Hekla to the east (Figure 1).

The SISZ is currently in a middle of an earthquake sequence. Two earthquake doublets struck in 2000 and 2008, with magnitude 6.5 and 6.0, respectively (Figure 1). The first *M*6.5 event on 17 June 2000 promoted failure of the fault that ruptured in a second *M*6.5 main shock on 21 June, located about 17 km to the west (e.g., Antonioli et al., 2006; Árnadóttir et al., 2003). The 29 May 2008 earthquakes were two magnitude 6 events that ruptured two parallel N-S right-lateral strike-slip faults (e.g., Decriem et al., 2010; Hreinsdóttir et al., 2009; Jakobsdóttir, 2008). From analysis of high-rate GPS data, Hreinsdóttir et al. (2009) argued that the second fault rupture was dynamically triggered within ∼3 s of the first main shock. The 21 June 2000 main shock increased Coulomb failure stress on N-S faults in the area of the May 2008 main shocks (Árnadóttir et al., 2003). Studies of the postseismic crustal deformation following the June 2000 main shocks indicate primarily viscoelastic relaxation, although some afterslip during the first 1–2 years cannot be ruled out (Árnadóttir et al., 2005;
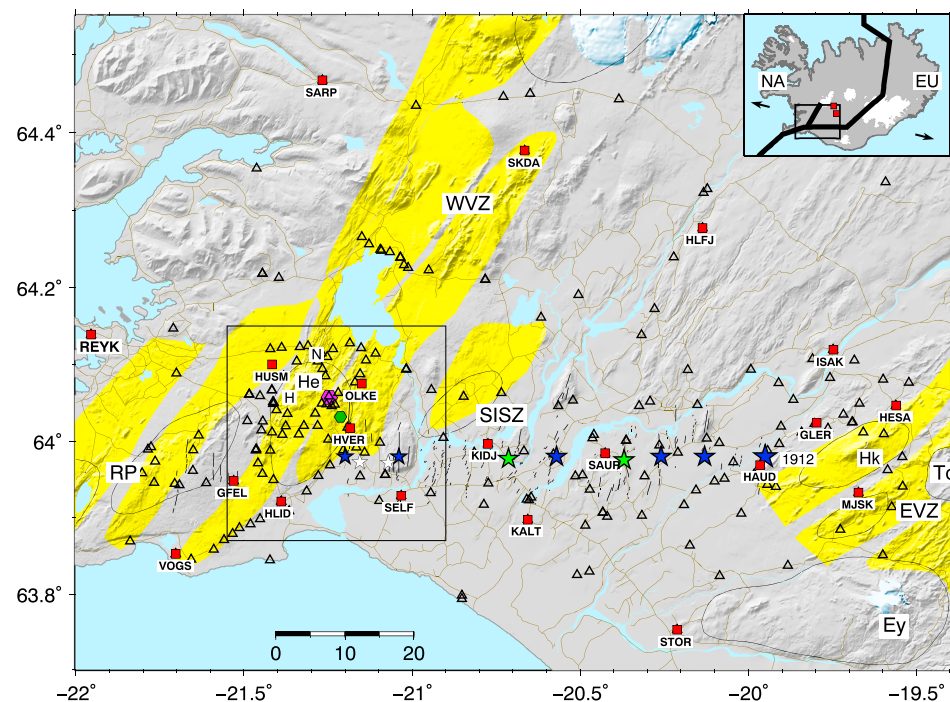
**Figure 1.** The main tectonic features in the study area: the Reykjanes Peninsula (RP), the Western and Eastern Volcanic Zones (WVZ and EVZ, respectively), and the South Iceland Seismic Zone (SISZ). The volcanoes Hengill (He), Hekla (Hk), Torfajökull (To), and Eyjafjallajökull (Ey) are labeled, as well as the two powerplants in the Hengill area, Nesjavellir (N) and Hellisheidi (H). Thin black lines are mapped surface faults (Clifton & Kattenhorn, 2006; Einarsson, 2008). The thin brown lines are roads. Main shock epicenters are indicated with stars: two M_w6.5 events the SISZ in June 2000 (green) and two M_w6 in western SISZ (Ölfus area) on 29 May 2008 (white). Estimates of locations of earlier main shocks (five M6–6.9 events in 1896 and a M7 in 1912) are shown with blue stars (Einarsson et al., 1981). Black open triangles are campaign GPS benchmarks observed in consecutive years so we can estimate station velocities during at least one time interval in our study. The red squares are continuous GPS stations, labeled with four-letter acronyms. A green hexagon marks the location of a center of inflation at ∼7-km depth in eastern Hengill estimated from interferometric synthetic aperture radar data spanning 1994–1998 (Feigl et al., 2000), and a purple hexagon marks the location of a similarly deep source of contraction obtained from GPS and interferometric synthetic aperture radar data during 2012–2015 (Juncu et al., 2017). The black box outlines the location of the western SISZ (Ölfus) and Hengill area. The inset shows a map of Iceland, with the plate boundary outlined with a thick black line, and the study area in the larger figure indicated with a box. The arrows indicate the direction of plate spreading across Iceland between the North American (NA) and Eurasian (EU) plates.

Decriem & Árnadóttir, 2012; Jónsson, 2008). Geodetic studies indicate that the main shocks in 2000 and 2008 released only half of the stored strain in the crust since the last major earthquake sequence in 1896–1912 (e.g., Árnadóttir et al., 2005; Decriem et al., 2010; Pedersen et al., 2003). Thus, magnitude 6–7 main shock(s) may be expected in South Iceland in the near future. A previous earthquake sequence during 1896–1912 initiated with five M6–6.9 events in the SISZ during 2 weeks in fall 1896 and culminated with a M7 main shock in spring 1912 in the eastern part of the zone (Figure 1), close to Hekla volcano (Bjarnason et al., 1993; Einarsson et al., 1981).

The Hengill central volcano is located at the Hengill triple junction that marks the western boundary of what is traditionally referred to as the SISZ. Hengill had an episode of increased seismicity and uplift of ∼20 mm/year during 1994 to 1998 (Feigl et al., 2000; Sigmundsson et al., 1997). The study by Feigl et al. (2000) interpreted the uplift via an inflating Mogi source at ∼7-km depth in the eastern part of Hengill (Figure 1). Since ca. 2000, there appears to be a wide area of subsidence in the Hengill region (Árnadóttir et al., 2005; Keiding et al., 2008) (and this study), which suggests a deep source of contraction. There are several high-energy geothermal fields in the Hengill area, which are currently harnessed by two power plants (Figure 1). The first one, at Nesjavellir, was commissioned in 1990. In 2006 a new larger plant started operation at Hellisheidi and the Nesjavellir plant was expanded. The extraction of geothermal fluids causes pressure decrease in the geothermal reservoirs and subsidence (Juncu et al., 2017). The subsidence observed by GPS and interferometric synthetic aperture radar
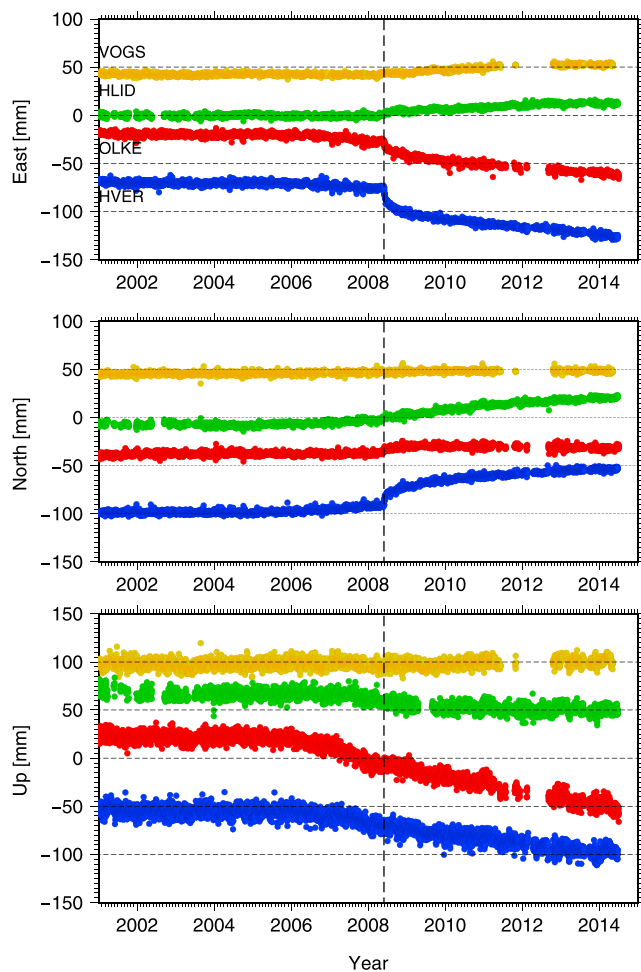
Figure 2. Time series showing the east, north, and vertical component of deformation at the continuous GPS stations in the Hengill and Ölfus area, during 2001–2015. VOGS is shown with yellow symbols, HLID is green, HVER is blue, and OLKE is red. The time series have been detrended; that is, a constant rate of deformation has been subtracted, and annual and semiannual signals have been removed. The data are also corrected for coseismic offsets in May 2008. The vertical line in 2008 indicates the time of the May 2008 main shocks. Uncertainties are less than 5 mm in horizontal and less than 10 mm in vertical.

(InSAR) during 2012–2015 has been modeled by a pressure decrease in three sources: two shallow ellipsoidal sources in the areas of fluid extraction and a deep spherical source at about 7-km depth located under the eastern part of Hengill, about 2 km SW of the CGPS station OLKE (Juncu et al., 2017). Reinjection of geothermal wastewater at the Hellisheidi power plant started in September 2011, causing swarms of induced earthquakes with two $M4$ earthquakes in October 2011 (Juncu et al., 2017).

The Hekla volcano is one of the most active volcanoes in Iceland, located near the intersection of the SISZ and the Eastern Volcanic Zone (EVZ; Figure 1). Before 1947, Hekla erupted roughly once every 100 years, but there have been five eruptions in the last century (1947, 1970, 1980–1981, 1991, and 2000; Höskuldsson et al., 2007; Thordarson & Larsen, 2007). Since the last eruption in February 2000 the volcano has been inflating (e.g., Ófeigsson et al., 2011). Early geodetic studies suggested a magma chamber at 5- to 10-km depth (e.g., Linde et al., 1993; Sigmundsson et al., 1992; Sturkell et al., 2006) based on spatially sparse data, but recent studies suggest a much deeper source (15–24 km; Árnadóttir et al., 2009; Geirsson et al., 2012; Ófeigsson et al., 2011).

GPS measurements in a geodetic network in South Iceland (see Figure 1) have been performed annually since June 2000, and a number of continuous GPS stations have been installed (e.g., Árnadóttir et al., 2006, 2005; Decriem & Árnadóttir, 2012; Geirsson et al., 2010; Keiding et al., 2008). The GPS measurements show that the plate boundary is a fairly narrow N-S trending zone, and dislocation models of the GPS station velocities suggest a locking depth of 10–15 km in the SISZ (e.g., Árnadóttir et al., 2006, 2009; Geirsson et al., 2012). Crustal deformation observed by GPS is most commonly shown as velocity vectors on maps and/or with time series plots. Surface deformation can, however, also be expressed as strain rates provided that the displacement field does not contain coseismic offsets—that is, the field must be continuous. Working with strain rates, which involve spatial derivatives of the GPS velocities, helps reveal interesting features in the geodetic data (Kreemer et al., 2014). In particular, we find it easier to infer spatial and temporal changes in the deformation from plots of strain rates compared to vector plots of the velocity field. Strain rates are also independent of the reference frame used to analyze the data.

Here we report GPS station velocities and strain signals in the SISZ, from measurements spanning 2001 to 2015. We apply a new method to estimate strain from GPS velocities: vertical derivatives of horizontal stress (VDoHS; Dimitrova et al., 2016; Haines et al., 2015). With VDoHS the strain signals are more finely resolved, smoother and less noisy than using conventional methods (Beavan & Haines, 2001). The goals of this study are to present these deformation measurements and strain calculations and demonstrate the temporal and spatial variation in these quantities. We use the surface velocities and strain rates to point out the most prominent sources of deformation in our study area and interpret the signals in the volcanic areas of Hekla and Hengill. Our study also indicates a significant increase in strain rates in the epicentral area of the May 2008 earthquakes, both prior to and following the main shocks.

2. GPS Data and Analysis

2.1. GPS Measurements

Annual campaign style GPS measurements have been conducted in the SISZ since June 2000 (Árnadóttir et al., 2006; Decriem et al., 2010; Juncu et al., 2017; Keiding et al., 2008). Figure 1 shows the network of campaign benchmarks and continuously operating GPS stations in South Iceland. The GPS data are analyzed using the MIT software GAMIT v10.6 (Herring et al., 2015), including data from over a hundred global reference stations, processed in house to ensure a uniform processing strategy for the local and global data. To
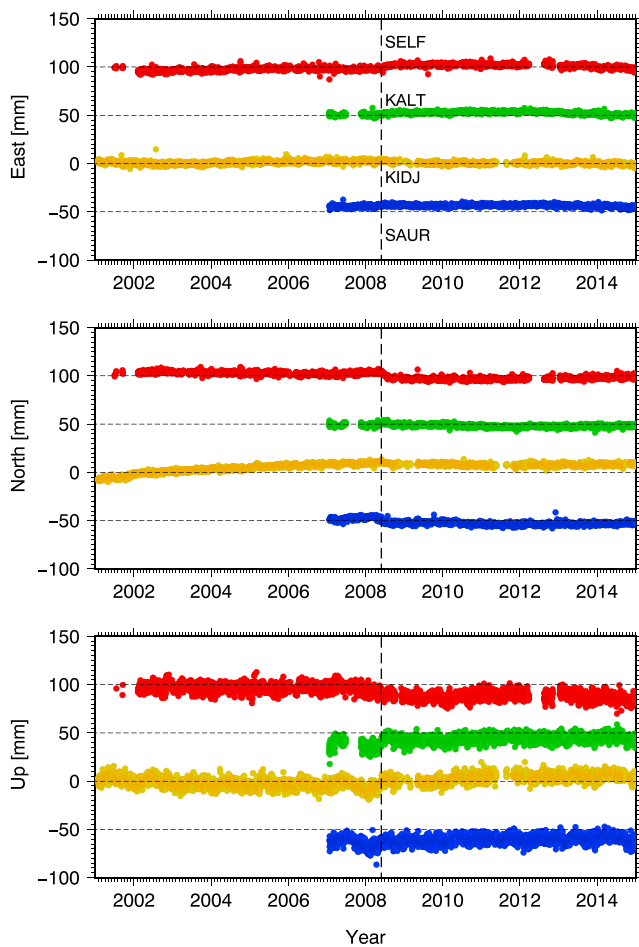
Figure 3. Time series showing the east, north, and vertical component of deformation at the continuous GPS stations in the South Iceland Seismic Zone, during 2001–2015. SELF is shown with red symbols, KALT is green, KIDJ is yellow, and SAUR with blue. The time series have been detrended; that is, a constant rate of deformation has been subtracted, and annual and semiannual signals have been removed. The data are also corrected for coseismic offsets in May 2008. The vertical line in 2008 indicates the time of the May 2008 main shocks. Uncertainties are less than 5 mm in horizontal and less than 10 mm in vertical.

minimize errors, we solve for the satellite orbits, Earth rotation parameters, and atmospheric zenith delay. We also apply the FES2004 model to correct for ocean tidal loading (Lyard et al., 2006) and the IGS08 azimuth and elevation-dependent absolute phase center models for the GPS and satellite antennas. The GPS station time series and velocities are then calculated from the station coordinates using GLOBK (Herring et al., 2015). The data analysis provides the GPS station locations, displacements, velocities, and the full data covariance for the estimated velocities in a global reference frame aligned with ITRF2008 (Altamimi et al., 2012). Finally, the station velocities are rotated to reflect motion relative to stable North America, using absolute angular velocities (see Table 3 in Altamimi et al., 2012).

Iceland Geosurvey (ISOR) has observed a dense network of GPS benchmarks in the Hengill area for the local power company, Reykjavík Energy (RE). Some of the benchmarks they measure are also included in the network observed by the Institute of Earth Sciences (IES). Their whole network is, however, not remeasured every year. The ISOR observation times tend to be short (8 hr) compared to the IES observations (a minimum of two full 24-hr sessions at each benchmark). All available GPS measurements done by ISOR for RE in Hengill (in 2001, 2002, 2003, 2005, 2006, 2007, 2008, 2009, and 2012) have been analyzed in the same manner as the IES campaigns in order to derive a detailed and consistent GPS velocity field for the study area.

2.2. GPS Time Series

We estimate the GPS station positions (east, north, and up) and plot as a function of time to generate time series of the motion. The time series are then used to calculate the station velocities. As examples, we show time series from four continuous GPS stations in the Hengill and Ölfus area (OLKE, HVER, HLID, and VOGS), from 2001 to 2015, in Figure 2, and four stations in the SISZ (SELF, KIDJ, KALT, and SAUR) in Figure 3. The locations of the stations are indicated in Figure 1. For display purposes, the time series have been detrended by subtracting constant velocities, from each component of motion, and corrected for coseismic offsets (Decriem et al., 2010) to enhance any transient signals.

The stations in the Ölfus area (Figure 2) show some temporal velocity changes, in particular, after the main shocks—that is, a change in slope after mid-2008. HVER has a rapid postseismic signal (in east and north) after 29 May 2008 until 2009 and also a longer-term velocity change, in particular, in slower eastward motion, after the main shocks. HVER also has a subtle increase in northward motion prior to the 29 May main shocks. The time series from OLKE show an increase in subsidence starting after 2006, contemporaneous with the start of a new power plant at Hellisheidi, and increased production at Nesjavellir (Juncu et al., 2017). The westernmost station (VOGS) shows a clear increase in eastward velocity following the 2008 main shocks. Similarly, an increase in northward motion is evident in the time series from HLID. Unfortunately, the stations VOGS, HVER, HLID, and OLKE were equipped with older GPS receivers that failed during 2014, causing extensive gaps in the time series after mid-2014.

The stations east of the 2008 main shocks (SELF, KIDJ, KALT, and SAUR) have more subtle, short-lived postseismic transients (Figure 3). SELF, located a few kilometers SSE of the 2008 main shocks, moves faster SE for a short time after the earthquakes. The most noticeable transient at KIDJ is northward postseismic motion after the June 2000 earthquakes, noted in an earlier study (Decriem & Árnadóttir, 2012).
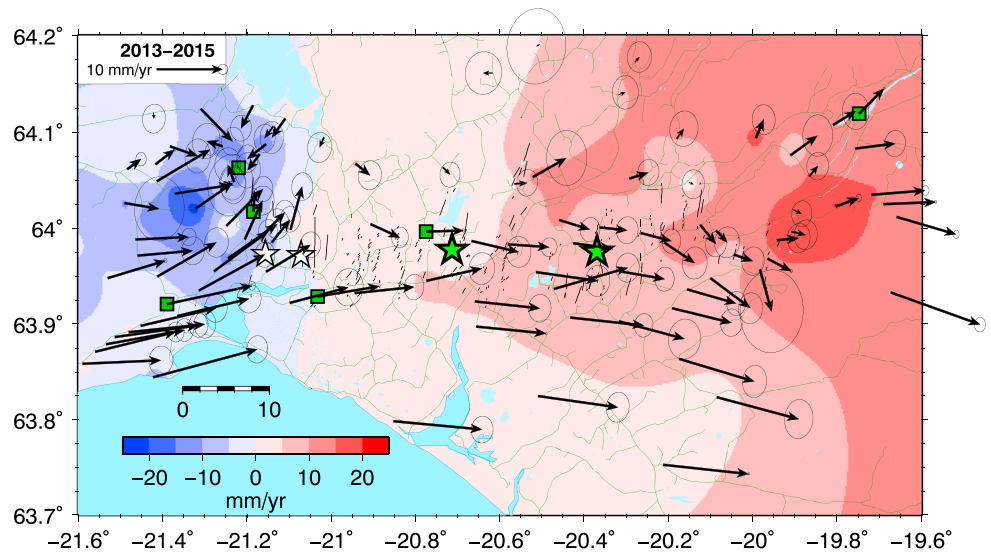
2.3. GPS Station Velocities

We calculate the GPS station velocities for several different time intervals based on examination of time series, data availability, and known events that have influenced crustal deformation in the study area. The main tectonic events are four M6+ earthquakes, two in June 2000 and two in May 2008. In order to obtain the best spatial and temporal coverage for deformation in the study area, we calculate GPS station velocities for
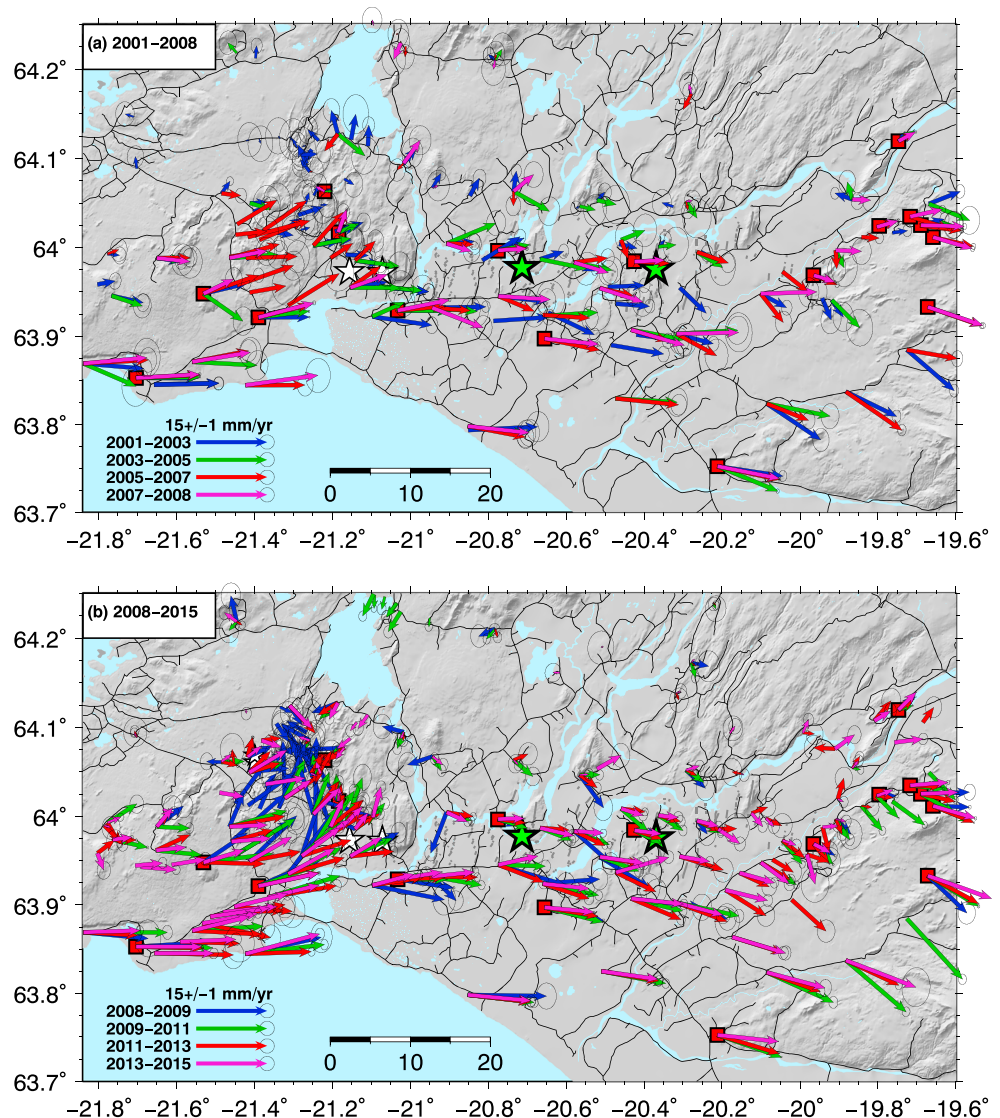
Figure 4. GPS station velocities in ITRF2008, relative to stable North America. The velocities are calculated for several 1- to 2-year time intervals (a) before and (b) after 29 May 2008. The velocities for the time intervals are shown with different colored arrows (68% confidence ellipses), as indicated in the figure legends. Stars show locations of $M > 5$ earthquakes.

several time intervals before the 29 May 2008 main shocks, that is, 2001–2003, 2003–2005, 2005–2007, and, 2007–2008 (Figure 4a), as well as following the 29 May 2008 main shocks, that is, 2008–2009, 2009–2011, 2011–2013, and 2013–2015 (Figure 4b). More detailed figures showing the GPS velocities and seismicity during the individual time intervals are included in the supporting information (Figures S1–S8). The time interval ending in 2008 includes data until 29 May, and the interval starting in 2008 is after 29 May, to avoid coseismic displacements due to the main shocks. The horizontal GPS station velocities are shown relative to stable North America in all the figures.

We find significant velocity variations, both in time and space during 2001–2015 (Figure 4). In general, GPS stations located in the northern and northwestern part of the study area have low velocities relative to stable North America, whereas the eastward component of velocity increases as we move southward across the plate boundary, onto the Eurasian plate. This pattern is perturbed in the Hengill area due to contraction and subsidence in the area of geothermal exploitation at two power plants (Nesjavellir and Hellisheidi). In addition to local subsidence in the Hengill area and uplift around Hekla, the vertical velocities indicate a broad E-W gradient across the area, with uplift in the eastern SISZ, influenced by the melting of the largest glaciers in Iceland (Árnadóttir et al., 2009). As an example, we plot both horizontal and vertical station velocities

Figure 5. Example GPS station velocities for the time interval 2013–2015, in ITRF2008. The vertical velocities are shown with the color scale (blue for subsidence and red indicates uplift), and the horizontal velocities (black arrows with 95% confidence ellipses) are relative to stable North America. We show only stations with uncertainties in horizontal and vertical velocities less than 5 and 10 mm/year, respectively. The green squares indicate continuous GPS stations. Thin green lines show roads. Other symbols are the same as in Figure 1.

during 2013–2015, with the vertical rates in color (Figure 5). See the supporting information for the other time intervals.

The horizontal velocities after 29 May 2008 in the area west of the main shocks are larger and have a more northerly direction than before (see, e.g., Figure 4b). The velocities in Hengill and Ölfus areas rotate gradually back to a more easterly direction and decrease in magnitude with time.

3. Strain Rates

3.1. VDoHS Method

We calculate the strain rates from the GPS station velocities using a new method, VDoHS, by Haines et al. (2015), and compare the results with strain rates estimated by an established method (e.g., Beavan & Haines, 2001; Haines & Holt, 1993). Haines et al. (2015) show that using the VDoHS method allows for a finer-resolution imaging of surface deformation than earlier methods (Beavan & Haines, 2001). We assume that the surface of the Earth behaves elastically and estimate the VDoHS rates by solving the horizontal component force balance equations, from the GPS velocities. The VDoHS rates are mathematically spatial derivatives of stress rates (Dimitrova et al., 2016; Haines et al., 2015) and are estimated using a Bayesian inference. Finer spatial resolution is obtained when the strain rates are estimated by integrating the VDoHS rates, rather than differentiating the GPS velocities as done before (Haines et al., 2015). This approach therefore removes the need for spatial smoothing used previously (Beavan & Haines, 2001; Haines & Holt, 1993; Kreemer et al., 2003). Also, the VDoHS rates fit the statistically significant variations in the GPS velocities, minimizing the influence of short wavelength noise (Dimitrova et al., 2016; Haines et al., 2015).

Here we summarize the method but refer the reader to Haines et al. (2015) for more details. For simplicity, we give the following equations for a flat Earth, whereas for the strain calculations shown in the subsequent sections we have used the solutions for a spherical Earth as given by Haines et al. (2015). The VDoHS method solves the force balance equations (see below) at the Earth's surface, assuming that the interseismic velocities are related to rates of change of stress (i.e., the crust is purely elastic). Then, the VDoHS rates can be estimated from the horizontal GPS velocities using elasticity theory.

For a flat Earth, the surface traction rates $\dot{\sigma}_{xz}$, $\dot{\sigma}_{yz}$, and $\dot{\sigma}_{zz}$ are 0. The force balance equations can be written as

$$\frac{\partial \dot{\sigma}_{xx}}{\partial x} + \frac{\partial \dot{\sigma}_{xy}}{\partial y} + \frac{\partial \dot{\sigma}_{xz}}{\partial z} = 0, \tag{1}$$

$$\frac{\partial \dot{\sigma}_{xy}}{\partial x} + \frac{\partial \dot{\sigma}_{yy}}{\partial y} + \frac{\partial \dot{\sigma}_{yz}}{\partial z} = 0, \tag{2}$$

and

$$\frac{\partial \dot{\sigma}_{xz}}{\partial x} + \frac{\partial \dot{\sigma}_{yz}}{\partial y} + \frac{\partial \dot{\sigma}_{zz}}{\partial z} + \frac{\partial (\rho g)}{\partial t} = 0. \tag{3}$$

We rewrite equation (3), since we cannot estimate the change in the gravitational force (ρg) from GPS velocities:

$$\dot{f}_z = \frac{\partial \dot{\sigma}_{zz}}{\partial z} + \frac{\partial (\rho g)}{\partial t}, \tag{4}$$

which is 0 at the surface in the flat Earth case. Similarly, we write the vertical derivatives of the horizontal stress (VDoHS) rates as follows:

$$\dot{f}_x = \frac{\partial \dot{\sigma}_{xz}}{\partial z}, \dot{f}_y = \frac{\partial \dot{\sigma}_{yz}}{\partial z}. \tag{5}$$

For an elastic medium we can write the horizontal stress rates as

$$\dot{\sigma}_{xx} = (\lambda + 2\mu)\frac{\partial u_x}{\partial x} + \lambda\frac{\partial u_y}{\partial y} + \lambda\frac{\partial u_z}{\partial z}, \tag{6}$$

$$\dot{\sigma}_{xy} = \mu\left(\frac{\partial u_x}{\partial y} + \frac{\partial u_y}{\partial x}\right), \tag{7}$$

$$\dot{\sigma}_{yy} = \lambda\frac{\partial u_x}{\partial x} + (\lambda + 2\mu)\frac{\partial u_y}{\partial y} + \lambda\frac{\partial u_z}{\partial z}, \tag{8}$$

where λ and μ are Lamé constants and u_x, u_y, and u_z are velocities in directions x, y, and z, respectively. At each point at the surface where there is elastic behavior, irrespective of the properties of the region below or at other surface points, we know that

$$\dot{\sigma}_{zz} = \lambda\frac{\partial u_x}{\partial x} + \lambda\frac{\partial u_y}{\partial y} + (\lambda + 2\mu)\frac{\partial u_z}{\partial z} = 0. \tag{9}$$

Rewriting this equation for u_z, we obtain the relationship between vertical strain and area strain:

$$\frac{\partial u_z}{\partial z} = -\frac{\lambda}{(\lambda + 2\mu)}\left(\frac{\partial u_x}{\partial x} + \frac{\partial u_y}{\partial y}\right). \tag{10}$$

Inserting equation (10) in equations (6) and (8), we can write $\dot{\sigma}_{xx}$ and $\dot{\sigma}_{yy}$ at the surface as follows:

$$\dot{\sigma}_{xx} = \frac{2\mu}{(1 - \nu)}\left(\frac{\partial u_x}{\partial x} + \nu\frac{\partial u_y}{\partial y}\right), \tag{11}$$

and

$$\dot{\sigma}_{yy} = \frac{2\mu}{(1 - \nu)}\left(\nu\frac{\partial u_x}{\partial x} + \frac{\partial u_y}{\partial y}\right), \tag{12}$$

where $\nu = \frac{\lambda}{2(\lambda + \mu)}$ is Poisson's ratio. Finally, using the above equations, we can write the horizontal component of the force balance equations at the surface as

$$\frac{\partial}{\partial x}\left[\frac{2\mu}{(1 - \nu)}\left(\frac{\partial u_x}{\partial x} + \nu\frac{\partial u_y}{\partial y}\right)\right] + \frac{\partial}{\partial y}\left[\mu\left(\frac{\partial u_x}{\partial y} + \frac{\partial u_y}{\partial x}\right)\right] + \dot{f}_x = 0, \tag{13}$$

$$\frac{\partial}{\partial x}\left[\mu\left(\frac{\partial u_x}{\partial y} + \frac{\partial u_y}{\partial x}\right)\right] + \frac{\partial}{\partial y}\left[\frac{2\mu}{(1 - \nu)}\left(\nu\frac{\partial u_x}{\partial x} + \frac{\partial u_y}{\partial y}\right)\right] + \dot{f}_y = 0. \tag{14}$$

The terms $\dot{f}_x$ and $\dot{f}_y$ are the VDoHS rates at the surface and the basis for the method by Haines et al. (2015) is solving equations (13) and (14). Here we consider only behavior at the Earth's surface, assuming that the crust deforms elastically, but we make no assumptions about the rheology at depth.

In the supporting information, we detail how we solve the horizontal force balance equations (equations (13) and (14)) at the Earth's surface, using the Haines et al. (2015) methodology. There are three groups of tasks: (1) constructing an expansion for the VDoHS rates based on the locations of GPS sites, (2) calculating

solutions to the force balance equations, separately for the far-field boundary conditions without internal sources of deformation (i.e., with $\dot{f}_x$ and $\dot{f}_y$ both 0), and for each individual source contribution in the expansion of VDoHS rates, and (3) inverting observed GPS velocities to obtain the coefficients in the expansion for VDoHS rates, using the calculated solutions to the force balance equations. The units for the force balance are force-per-unit-time-per-unit-volume of an infinitesimally thin layer. A standard value of Poisson's ration of 0.25 is assumed in the following analysis.

Sandwell and Wessel (2016) have produced a simplified variant of our method called *gpsgridder* that is now available as part of the Generic Mapping Tools (Wessel et al., 2013). The two methods handle the tasks differently. The Haines et al. (2015) approach is more generally applicable, but gpsgridder is a useful and computationally cheaper alternative for data sets that are approximately uniformly distributed and where what happens outside the immediate vicinity of the GPS locations is unimportant. The first of these requirements means that the gpsgridder option is not suitable for the data sets analyzed in this paper because the GPS observations are quite irregularly spaced. Between the two approaches there are, however, many other possibilities for performing the tasks, pulling together parts of one with parts of the other, or substituting different ways to handle one or more of the tasks. So long as the force balance equations are used legitimately, with VDoHS rates that are spread to match the spacing of the GPS data (avoiding such things as putting very localized sources where there is no evidence for them), the fitted solutions (especially velocities and strain rates) will be effectively the same: The key point is that the horizontal force balance equations at the Earth's surface are powerful constraints.

3.2. Strain Rates in SISZ

We estimate the VDoHS rates and strain rates for the same eight time intervals as the GPS velocities (2001–2003, 2003–2005, 2005–2007, 2007–2008, 2008–2009, 2009–2011, 2011–2013, and 2013–2015). Figure 6 shows the areal strain rates in the study area, as a function of time. Warm colors (green, yellow, and red) indicate dilatation (positive strain) and cold colors (light to dark blue) represent contraction (negative strain). The arrows show the VDoHS rate field as vectors, for example, pointing toward sources of contraction such as in the Hengill area or away from a source of expansion in the case of Hekla. We find that the highest rate of contraction (negative strain) is in the western part of the SISZ, that is, in the Hengill area, decreasing with time from about −0.1 microstrain per year in 2001–2003 to about −0.6 microstrain per year in 2005–2007, and larger than −1 microstrain per year after 2008, with a halo of extension in the surrounding area (Figure 6). This is consistent with an increase in geothermal exploitation in the area. A new plant (Hellisheidi) started operating in 2006, and production has been increasing at Nesjavellir, causing more subsidence and contraction due to extraction of geothermal fluids (Juncu et al., 2017). Another prominent source of areal strain, in this case dilatation (positive strain), is located in the eastern part of the SISZ, around Hekla volcano (Figure 6). The magnitude of the dilatation is fairly constant with time after 2003 (∼0.3–0.6 microstrain per year). The highest rate is during 2001–2003, possibly indicating a high rate of magma recharge after the February 2000 Hekla eruption or viscoelastic reajustment following the eruption (Segall, 2016). The VDoHS vectors point away from the center of the signal. This and the persistent dilatational strain confirm that magma is accumulating below the volcano since the eruption in 2000, also noted by dry-tilt measurements west of Hekla (Sturkell et al., 2013). The wide area of dilatation we observe is consistent with recent geodetic studies, which estimate a magma chamber(s) at 15- to 25-km depth below Hekla (Geirsson et al., 2012; Ófeigsson et al., 2011; Sturkell et al., 2013). Further analysis of the strain signal at Hekla is performed in section 5.2.

There are subtle areal strain signals in the epicentral areas of the June 2000 main shock—a four lobed pattern (contraction in the NW and SE quadrants and extension in the SW and NE) that reflects postseismic deformation after 2001 (Figure 6a). This signal is small (∼ ±0.1 microstrain per year) and decreases with time. This is consistent with studies showing that the two main earthquakes in June 2000 ruptured N-S, right-lateral strike-slip faults, and postseismic deformation indicate primarily viscoelastic relaxation (Árnadóttir et al., 2005; Jónsson, 2008). The areal strain rates in the May 2008 epicentral area during 2008–2009 are large (more than ±0.5 microstrain per year) and have significant areal extent with a similar pattern as observed after June 2000—contraction in the NW and SE quadrants and extension in the SW and NE (Figure 6e).

The shear strain rate is generally high in the SISZ during 2001–2008 (0.5–1 microstrain per year) as evident in Figure 7. During 2001–2003 the highest rates are in the epicentral areas of the June 2000 main shocks (0.8–1 microstrain per year), decreasing with time. From the first time interval (2001–2003) there is a persistent shear strain anomaly in the epicentral area of the May 2008 main shocks (purple stars in Figure 7).
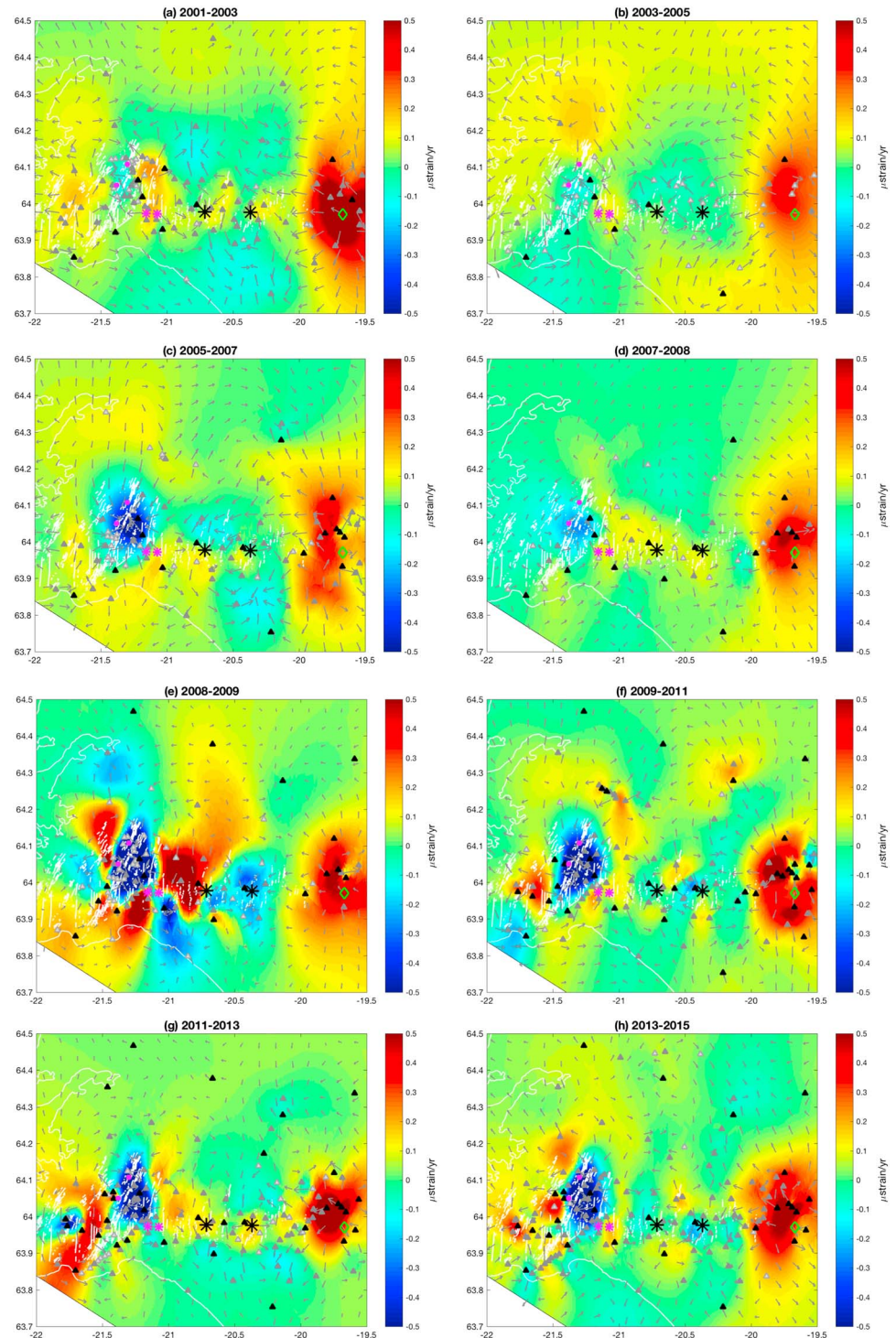
Figure 6. Areal strain rates calculated from GPS station velocities: (a) 2001–2003, (b) 2003–2005, (c) 2005–2007, (d) 2007–2008, (e) 2008–2009, (f) 2009–2011, (g) 2011–2013, and (h) 2013–2015. The red colors indicate dilatation, and the blue colors represent contraction (microstrain per year). The vectors show vertical derivatives of horizontal stress rate (scaled). The GPS station locations are shown with filled triangles, color coded according to the standard error: Black is less than 0.5 mm/year, gray is between 0.5 and 1.5 mm/year, and light gray is greater than 1.5 mm/year. The epicentral locations of the June 2000 and May 2008 main shocks are shown with black and purple stars, respectively. The location of the summit of Hekla volcano is indicated with a green diamond, and the two purple squares are the locations of the geothermal power plants in Hengill.
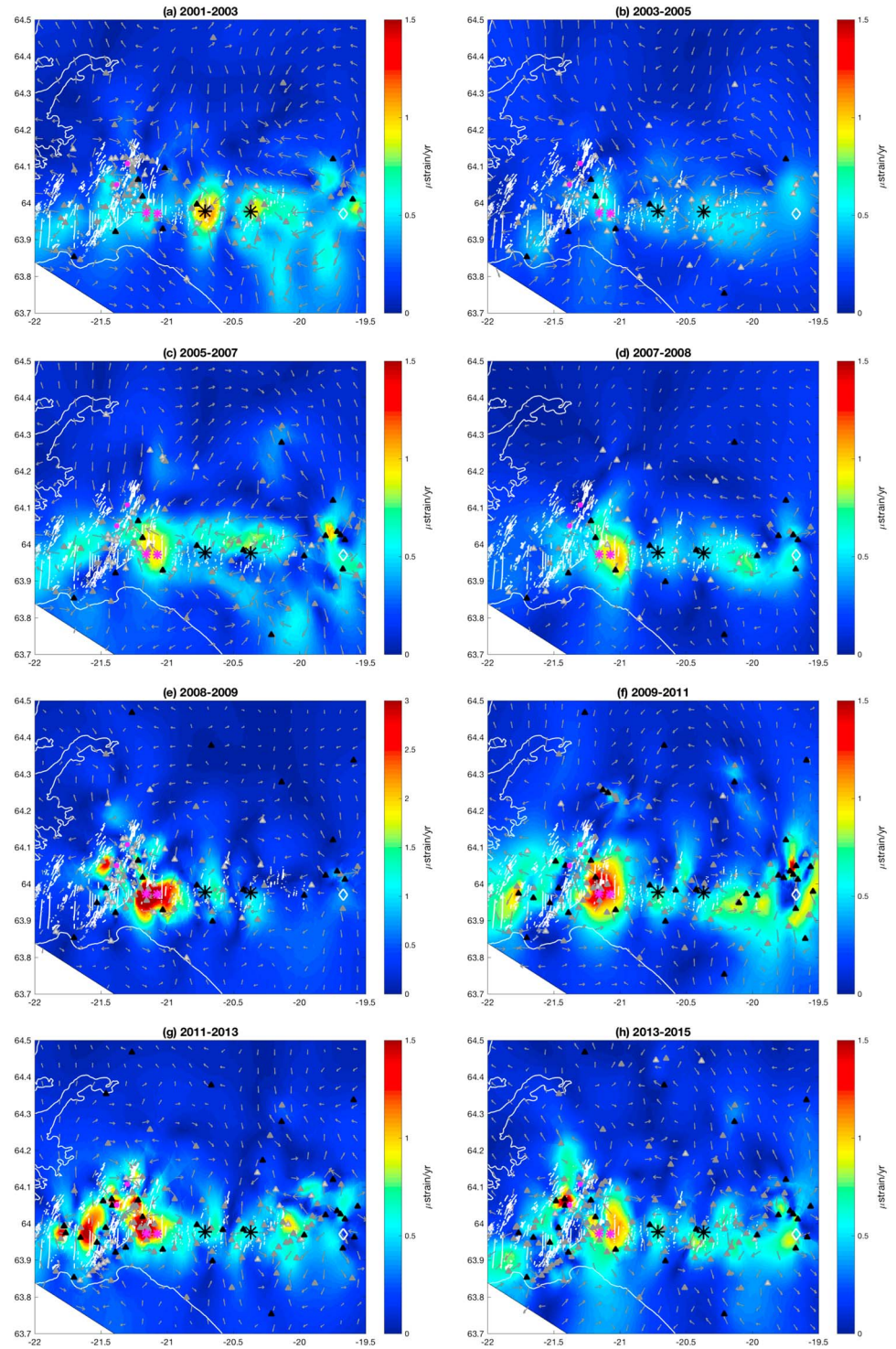
Figure 7. Shear strain rates calculated from GPS station velocities: (a) 2001–2003, (b) 2003–2005, (c) 2005–2007, (d) 2007–2008, (e) 2008–2009, (f) 2009–2011, (g) 2011–2013, and (h) 2013–2015. The color scale represents the magnitude of shear strain in microstrains per year. Note that the color scale for the shear strain in 2008–2009 (d) is different from the other years, due to very high shear strain rates. The location of the summit of Hekla volcano is indicated with a white diamond. Other symbols are the same as in Figure 6.
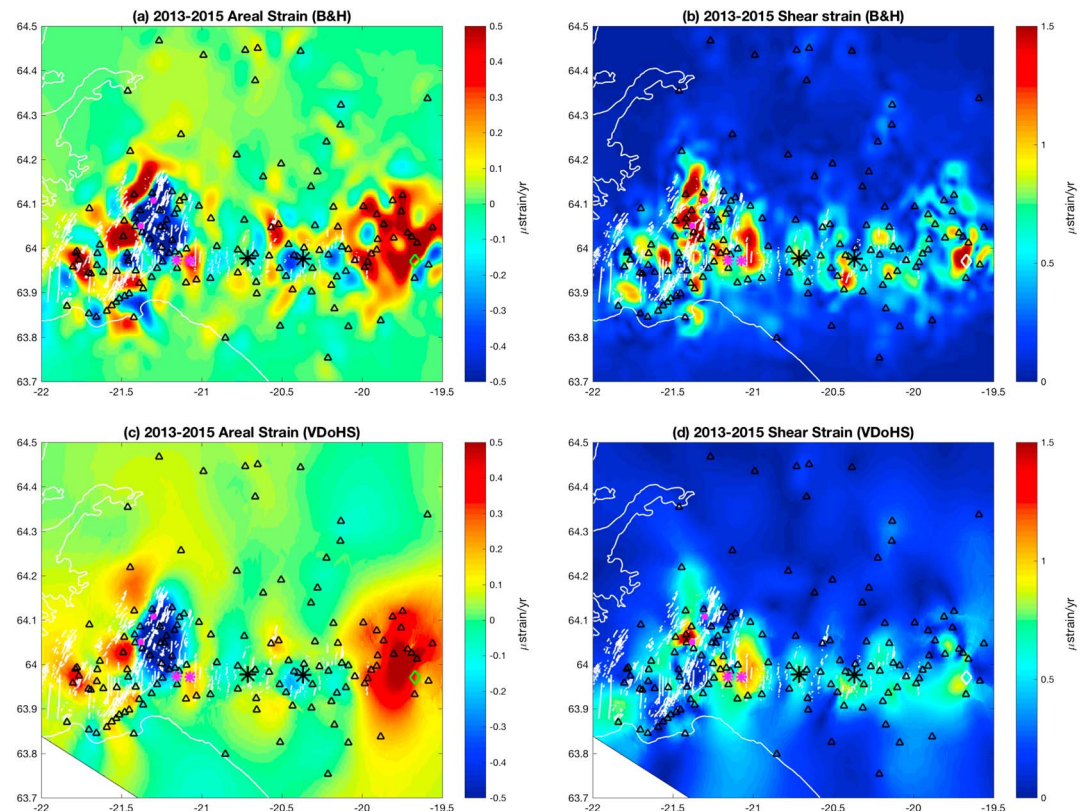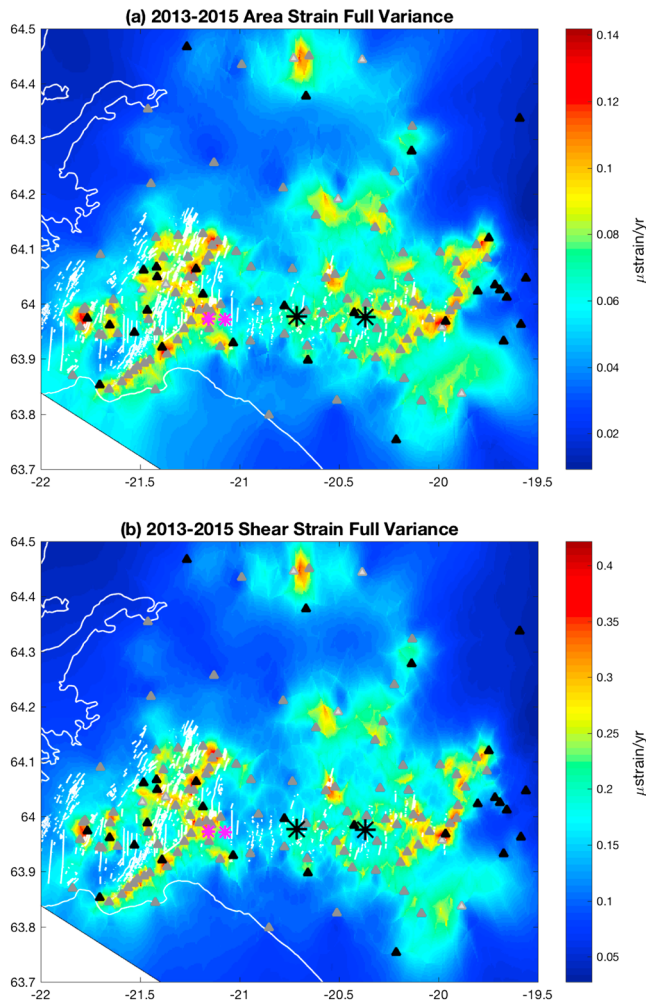
Figure 8. Shear strain rates calculated using the method of (a and b) Beavan and Haines (2001) and (c and d) VDoHS method, for the time period 2013–2015. Panels (a) and (c) show the areal strain rates, and panels (b) and (d) are the shear strain rates. The color scale represents the magnitude of strain in microstrains per year. Open triangles depict the GPS station locations. Other symbols are the same as in Figures 6 and 7.

This shear strain signal increases both in areal extent and magnitude with time. During 2007–2008, *before* the May 2008 main shocks, the shear strain rates exceed 1 microstrain per year in Ölfus (Figure 7d). In the first year following the Ölfus main shocks (2008–2009), the shear strain rates are very high (up to 6 microstrains per year) in the 2008 epicentral area (Figure 7e). It is interesting to note that the shear strain rates in the June 2000 epicentral areas also increase during this time interval, indicating further adjustment in these areas. The shear strain rates remain high around Hengill (>1.5 microstrains per year) during the remainder of the period under study (through end of 2015). The shear strain rates are also elevated in the eastern part of the SISZ (~0.7–1 microstrain per year) during the later part of the study period (Figures 7f–7h). The areas with the highest shear strain rates after 2008 correspond to areas of persistent microseismicity—including continued aftershock activity in the May 2008 epicentral area, induced seismicity in western Hengill (with two *M*4 events in 2011), and swarm activity in 2012 in Bláfjöll and in the eastern part of the SISZ (Figure S7).

3.3. Comparison of VDoHS and Established Methods

We also calculate the strain rates using the established method of Beavana nd Haines (2001; see Figure 8 and the supporting information). As with the VDoHS method, the contraction in Hengill and expansion in the Hekla area are evident. In general, the strain rates obtained using the established method agree fairly well with the strain rates estimated from the VDoHS rates, although the signals using the method of Beavan and Haines (2001) are *noisier* (i.e., more localized areas with high strain rate magnitudes). For example, both methods find a persistent shear strain anomaly in the epicentral area of the 2008 main shocks, starting as early as 2001–2003 and increasing in strength with time, as well as major changes in the strain rates post-2008 (see Figure 7 and supporting information Figure S14). We find, however, that the solutions are less stable for the strain rates using Beavan and Haines (2001), in particular, after the May 2008 main shocks. The level of fit we choose affects

Figure 9. Standard error estimate for (a) areal strain rates and (b) shear strain rates calculated from vertical derivatives of horizontal stress rates for 2013–2015. The standard error is calculated from the full covariance. The color scale has units of microstrains per year. The GPS station locations are shown with filled triangles, color coded according to the standard error: Black is less than 0.5 mm/year, gray is between 0.5 and 1.5 mm/year, and light gray is greater than 1.5 mm/year. The epicentral locations of the June 2000 and May 2008 main shocks are shown with black and purple stars, respectively.

the final strain rates we estimate, as the GPS velocities show high level of spatial variation. This demonstrates the difficulty in using conventional methods to estimate strain rates in our study area. Therefore, we maintain that it is advantageous to use the VDoHS method where we aim to look for possible (subtle) strain anomalies, such as in the SISZ.

4. Error Analysis

In the previous section, we demonstrate that details of the strain rate fields we estimate from GPS velocities can depend on the method used (see Figure 8). Hence, it is important to discern the signal from the noise. In this section, we will briefly explain how the standard errors are estimated for the strain rates derived with the VDoHS method and refer the interested readers to a more full description in the supporting information and Haines et al. (2015). Note that here errors relate to a question of *what is* dictated by the limitations of the data in terms of accuracy of the results, whereas uncertainty relates to *what if* there were many more data, including with what precision currently hidden details of the deformation could be illuminated. We will only address the issue of errors in this section.

The standard errors we present for VDoHS strain rates are derived from the covariance matrices for a posteriori conditional probability density $p(\mathbf{m}|\mathbf{d})$ in the inversion methodology described in detail by Haines et al. (2015). Here $\mathbf{m}$ is the model consisting of VDoHS rates at primary nodes of triangulation grids based on GPS sites and $\mathbf{d}$ is the data vector consisting of the observed GPS velocities. To obtain fitted velocities and strain rates, forward modeled basis solutions related to Green's functions are calculated for continuously distributed VDoHS rate basis function surface sources, one for each primary node and for each component of VDoHS rate.

Let us denote a set of model parameters derived from $\mathbf{m}$ as $\mathbf{p}$. These could be fitted velocities, strain rates, or VDoHS rates at any set of points, with the corresponding forward modeled basis solutions being a matrix G (for Green's function) such that $\mathbf{p} = G\mathbf{m}$. Note that $\mathbf{m}$ itself is a particular example, where $\mathbf{p}$ is the VDoHS rates at the primary nodes, and that in this case G is the identity matrix. Another example is where $\mathbf{p}$ is the predicted velocities at the GPS sites. To aid the reader, we provide a list of the parameters and their vector dimensions (see the supporting information).

Using the notation of Haines et al. (2015), the covariance matrix in the conditional probability density $p(\mathbf{m}|\mathbf{d})$ for $\mathbf{m}$ given $\mathbf{d}$ is

$$\left[A^T W_d A + C_m^{-1}\right]^{-1}. \tag{15}$$

A is the form of G relating $\mathbf{d}$ to $\mathbf{m}$, W_d is the weight matrix (inverse of data covariance) for the misfit between $\mathbf{d}$ and the fitted velocities $A\mathbf{m}$, which is the corresponding vector of fitted velocities in the joint probability density for $\mathbf{m}$ and $\mathbf{d}$, and C_m is the covariance matrix for $\mathbf{m}$ in its marginal probability density. The construction of the joint probability density for $\mathbf{m}$ and $\mathbf{d}$ is summarized in the supporting information and explained in detail by Haines et al. (2015). The associated covariance matrix in the conditional probability density $p(\mathbf{p}|\mathbf{d})$ for $\mathbf{p}$ given $\mathbf{d}$ is $G\left[A^T W_d A + C_m^{-1}\right]^{-1} G^T$, which comes from the general relationship cov($\mathbf{y}$)=B cov($\mathbf{x}$)B^T between covariance matrices of linearly related vectors $\mathbf{x}$ and $\mathbf{y}$ such that $\mathbf{y} = B\mathbf{x}$. This is the covariance form, with G as the strain rate basis solutions, used to calculate the (a posteriori) standard errors for strain rates.

The standard errors for the area strain rate and shear strain rate during 2013–2015 are shown in Figure 9, as an example. Supporting information Figures S10 and S11 depict the standard errors for all the time intervals. Given that our data set consists of observed velocities at GPS sites, the fitted strain rates are essentially no more than mutually consistent average strain rates between those sites. Consequently, their standard errors are highest where the GPS sites are close together (see the supporting information).
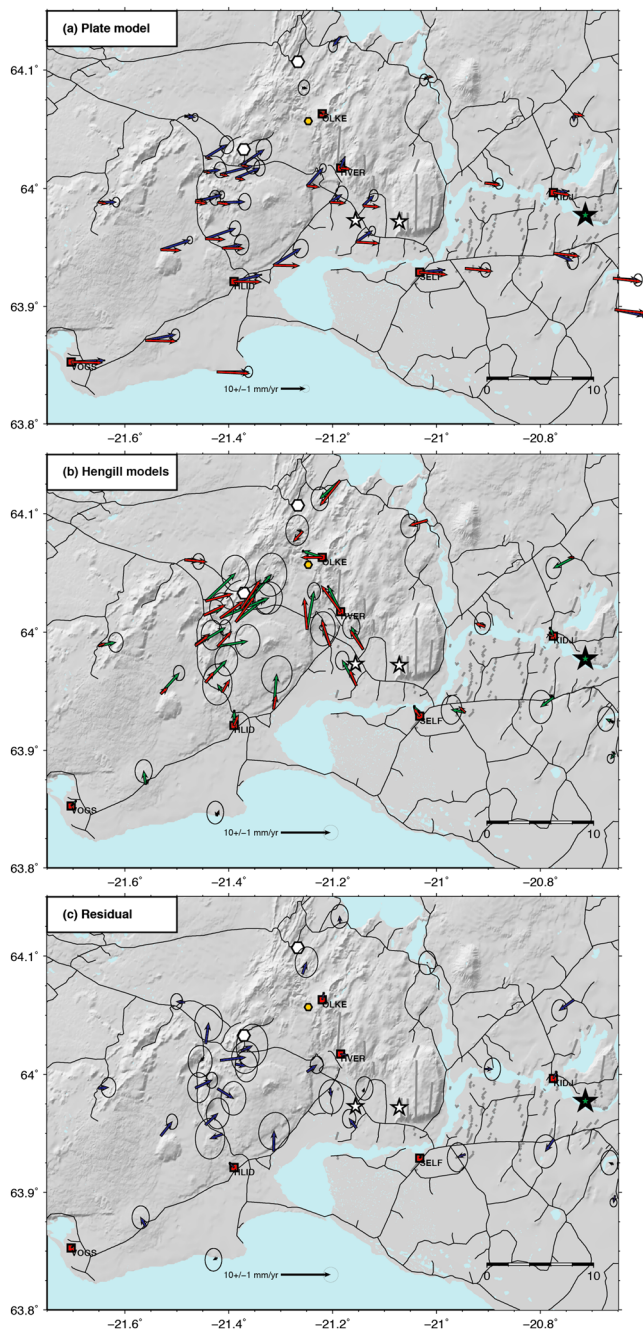
Figure 10. (a) Observed GPS station displacements in the Ölfus area during 2005–2007 (blue arrows with one sigma confidence ellipses) and motion predicted from a plate spreading model (red arrows). (b) Residual velocities after subtracting the plate model (green arrows), compared with predicted motion (red arrows) for model of deformation due to extraction of geothermal fluid from two shallow reservoirs (large white hexagons) and a deep contracting source (small yellow hexagon) in Hengill (Juncu et al., 2017). (c) Residual motion after subtracting motion predicted by plate model and contracting sources in Hengill. Note the velocity scale in (b) and (c) are twice that of (a). Other symbols are the same as in Figure 1.

In general the standard errors for the areal strain are small (0.1 microstrain per year), compared to the areal strain signal (± 0.5 microstrain per year), before the May 2008 earthquakes. There is an increase in the standard error, to ~0.15–0.3 microstrain per year, in the Ölfus area after the May 2008 main shocks, reflecting the denser GPS network observed following the earthquakes. These error analyses indicate that areal strain rates larger than ~0.1 microstrain per year are, for the most part, above the noise level. The largest areal strain signals are dilatation in the Hekla area and contraction in the Hengill area after 2005, on the order of ± 0.5 microstrain per year, respectively.

The standard errors for the shear strain rates are ~0.3–0.4 microstrain per year, except that in the western Hengill area during 2008–2009, they increase locally to ~1 microstrain per year. The shear strain rates are larger than ~0.5 microstrain per year in the SISZ, where the standard errors are ~0.3 microstrain per year, for the most part. In particular, the standard errors are ~0.2–0.3 microstrain per year prior to the May 2008 earthquakes, whereas the strain rates are 0.5–1.0 microstrain per year in the epicentral area. Therefore, we conclude that the shear strain signal is above the standard error in the areas and time intervals of interest.

5. Results and Modeling

5.1. Strain in the Epicentral Area Prior to the May 2008 Earthquakes

The strain anomaly in the epicentral area of the May 2008 earthquakes is enigmatic. It is evident prior to the main shocks, increasing with time from 2001 up to May 2008 (Figures 7a–7d). The deformation in the Ölfus area is due to plate spreading, subsidence in the Hengill area, and postseismic transients following the June 2000 and May 2008 earthquakes. Here we focus on the period 2005–2007 to minimize postseismic signals from the June 2000 main shocks, in order to investigate what processes can explain the strain signal prior to May 2008.

Plate spreading across the Hengill triple junction causes surface deformation and strain in the Ölfus area. To remove the signal of secular plate motion, we use a model obtained by Árnadóttir et al. (2009) for a country wide GPS velocity field during 1993–2004. It should be noted that the plate motion estimated by Árnadóttir et al. (2009) has a very sparse network in the Hengill area and includes an episode of uplift in Hengill during 1994–1998. Therefore, we use the same geometry of the plate boundary but exclude the inflating source in Hengill. We assume a rate of strike slip along the Reykjanes Peninsula and the SISZ of 16 mm/year below a locking depth of approximately 5 and 8 km, respectively, and a rate of opening along the Reykjanes Peninsula and the Western Volcanic Zone of 5 mm/year below 5-km depth. We calculate the predicted displacements at all the GPS stations in the area and compare the observed velocities during 2005–2007 with the model prediction (Figure 10a). The difference between the observed and predicted displacements is shown in Figure 10b. After subtracting the plate motion, the station velocities are primarily directed toward Hengill. This is consistent with a recent study by Juncu et al. (2017), where the subsidence in the Hengill area observed by GPS and InSAR during 2012–2015 is modeled by pressure decrease in two shallow geothermal reservoirs due to exploitation and a deeper (~7 km) contracting source. The rates of extraction are much lower at Hellisheidi for the time interval 2005–2007 (8 Mton/year) compared to 38 Mton/year during 2012–2015 used in the study of Juncu et al. (2017) but similar at Nesjavellir (13 Mton/year in 2005–2007 and 16 Mton/year for 2012–2015). We calculate the predicted displacements for the GPS stations in Hengill using the model from Juncu et al. (2017),
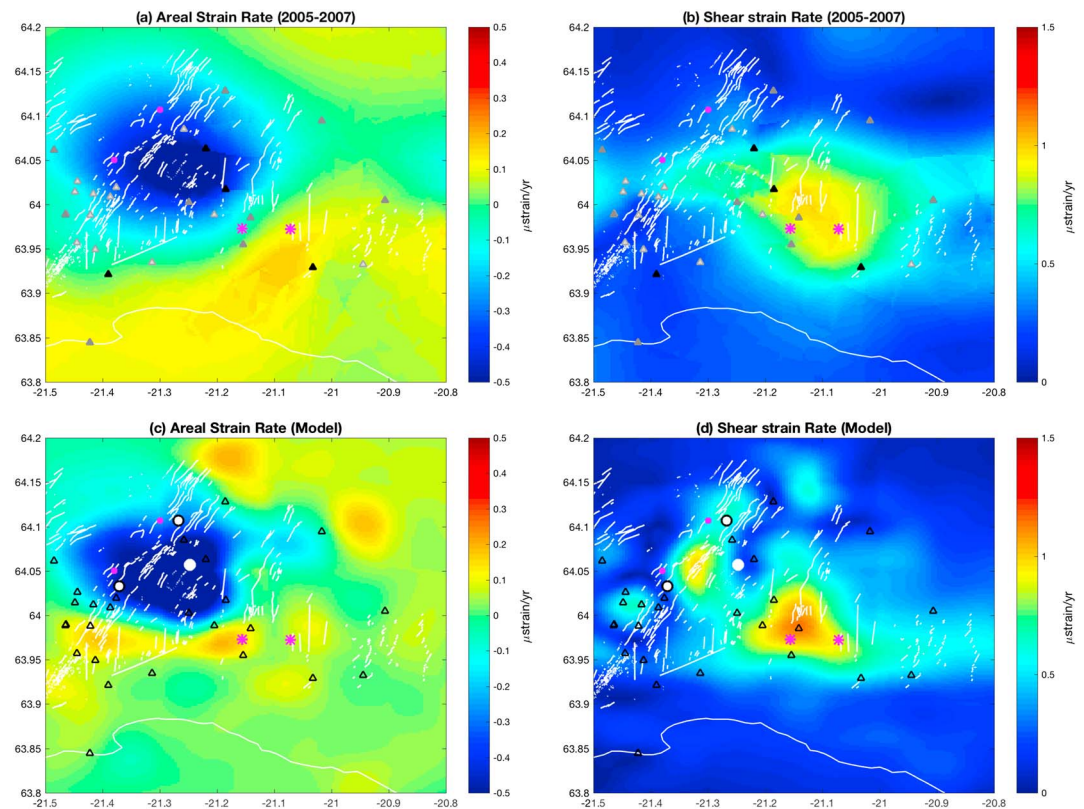
Figure 11. Strain rates in the Ölfus area during 2005–2007. (a) Areal strain rate and (b) shear strain rate estimated from observed GPS station velocities during 2005–2007. (c) Areal strain rate and (d) shear strain rate estimated from models of plate motion and contraction and subsidence in the Hengill area. The color scales show the strain rates in microstrains per year. Negative areal strain rate (cold colors) indicates contraction, and positive (warm colors) denotes dilatation. The triangles show the GPS station locations. The purple stars are the epicentral locations of the 29 May 2008 main shocks. The white circles indicate the locations of two shallow geothermal sources (smaller circles) and a deep (~7 km) source (large circle) in Hengill (Juncu et al., 2017).

adjusting the pressure drop for the Hellisheidi reservoir to reflect lower extraction rates in during 2005–2007. For the most part, the velocities from the Hengill models are similar to the velocities corrected for plate motion (Figure 10b). After subtracting the motion predicted by the contracting sources in Hengill, most of the final residual velocities are within 1σ of the data uncertainties (Figure 10c).

We also compare the strain signal from the observed GPS station velocities during 2005–2007, using the VDoHS method, with that for our model of plate motion and contraction in the Hengill area estimated from the established method by Beavan and Haines (2001), assuming noiseless data with uniform standard errors. The observed and predicted areal strain rates (Figures 11a and 11c) show an extensive signal of contraction in the Hengill area (larger than −0.5 microstrain per year) and a subtle extension in the areas surrounding Hengill (up to 0.2 microstrain per year). The extension includes the epicentral area of the May 2008 main shocks. The observed and predicted shear strain rates (Figures 11b and 11d) indicate significant shear strain in the epicentral area (~1.0 microstrain per year).

Most of the strain signal calculated from the 2005–2007 velocities can therefore be explained by a model of plate motion and sources of contraction in the Hengill area. The contraction may have decreased the normal stress on N-S oriented faults in Ölfus, promoting failure on the faults that ruptured on 29 May 2008. A denser data set is, however, needed to discern whether temporal variation and/or additional sources in the area contribute to the apparent increase in shear strain with time.

5.2. Using VDoHS Rates to Detect Volcano Deformation
The strong dilatational strain signal around Hekla suggests an inflating magma source. Many geodetic studies of Hekla have been conducted, but estimating depth and volume of magma accumulation below Hekla is difficult as the volcano is located at the eastern end of the SISZ, in an active seismic zone, and adjacent to the
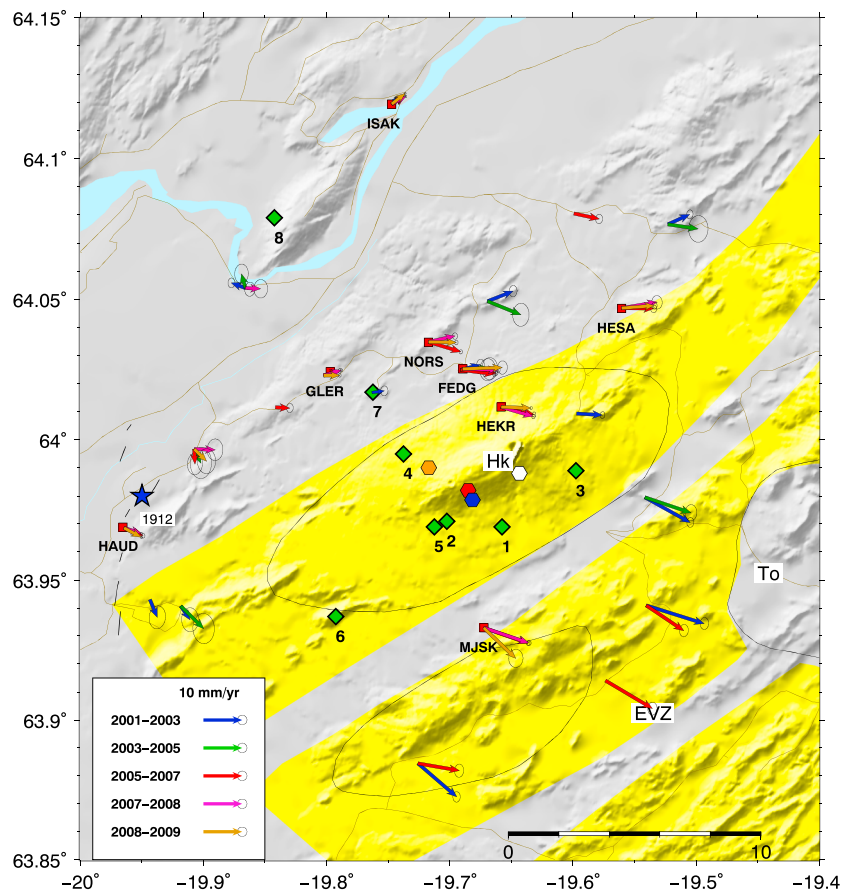
Figure 12. Map of the Hekla area with GPS station velocities (colored arrows) and estimated locations of inflation source(s) during 2001–2009. Average location of an inflating source under Hekla (blue hexagon) from vertical derivatives of horizontal stress rates (63.9786, −19.6815). Estimates of locations of inflation sources for each time interval (green diamonds), the numbers refer to the different time intervals (1: 2001-2003; 2: 2003–2005; 3: 2005–2007; 4: 2007–2008; 5: 2008–2009; 6: 2009–2011; 7: 2011–2013; 8: 2013–2015). The white hexagon is the location of the optimal source of deflation and inflation estimated from InSAR data during 1993–2008 by Ófeigsson et al. (2011). The red and orange hexagons are locations of optimal models (an inflating ellipsoid and spheroid, respectively) from GPS data spanning 2000–2010 by Geirsson et al. (2012). The blue star indicates the location of the 1912 *M*7 earthquake. Continuous GPS stations are labeled with station names. Other symbols are the same as in Figure 1. See also Table 1. EVZ = Eastern Volcanic Zone.

EVZ, an area of extension and active volcanism. Furthermore, the melting of the glaciers in Iceland produces uplift over a broad area, due to glacial isostatic adjustment (GIA; Árnadóttir et al., 2009). The GIA causes uplift through the SISZ, increasing from west to east (Figure 5)

In this section, we investigate the possibility of using the VDoHS rates to estimate the location of the inflating source and the areal strain rates to find the depth and volume change. By focussing on the areal strain and subtracting a background areal strain signal, we bypass the difficulty of estimating the many additional model parameters that are needed to correct the GPS velocities for the plate motion, GIA signal, and magmatic activity in the EVZ. As the focus of this study is the SISZ, and since we wanted to minimize the signal from the 2010 Eyjafjallajökull eruption (Sigmundsson et al., 2010), we have not included data from GPS stations east of Hekla. In turn, this may bias our estimates of the location of the dilatation signal in the Hekla area.

First, we derive a relationship between the VDoHS rates and the depth to a Mogi source (Mogi, 1958; see the supporting information), and then we apply it to Hekla. We use the minimum of the VDoHS rates to find the locations of the source(s) at Hekla and the areal strain rates to estimate source depths and volume change. We estimate these locations for the individual time intervals (see Figure 12 and supporting information Figures S16 and 17). We find that the local minimum of the VDoHS rates is in the same area for the first five time periods, and there is no systematic temporal variation in the locations until 2009–2011 (Figure 12). After 2009–2011,
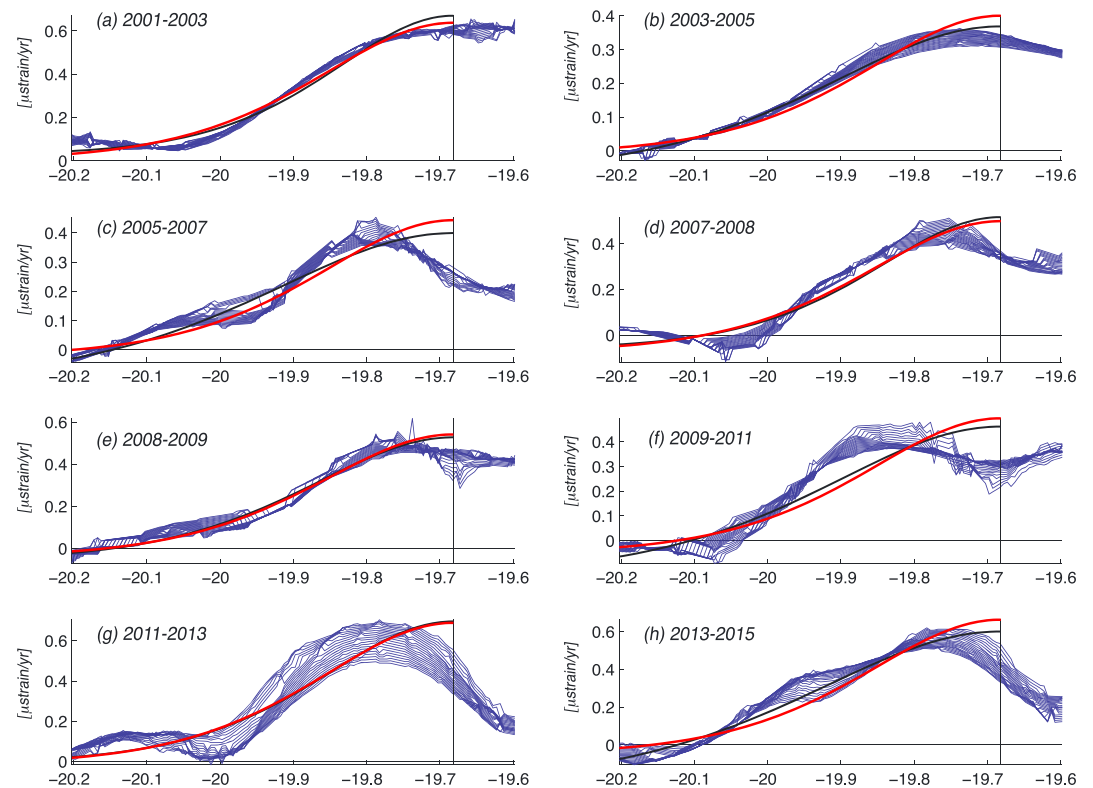
Figure 13. East-west profiles of areal strain rates across the South Iceland Seismic Zone and Hekla area for the eight time intervals: (a) 2001–2003, (b) 2003–2005, (c) 2005–2007, (d) 2007–2008, (e) 2008–2009, (f) 2009–2011, (g) 2011–2013, and (h) 2013–2015. The vertical axis shows the areal strain rates in microstrains per year, and horizontal axis is longitude (in degrees from west to east). Observed areal strain rates, that is, calculated from the vertical derivatives of horizontal stress rates are shown with thin blue lines. The 44 profiles are plotted from the areal strain rates shown in Figure 6, at different latitudes. The best fit models with the source depth estimated for each time interval are indicated by a thick black line, while the thick red line shows the model assuming a fixed source depth. Each model profile is plotted for an E-W profile at the latitude of the best fit location. The vertical black lines show the average source location estimated for all the time intervals (see Figure 12).

we find locations that are scattered outside the Hekla central volcano, and we suspect the strain rates are affected by the 2010 Eyjafjallajökull eruption. Hence, we estimate an average source location for the first five time intervals (2001–2009) at 63.9786°N and 19.6815°W and assume that the inflation remains at this position for the subsequent analysis. This location agrees well with estimates from recent geodetic studies of Hekla (see Figure 12). Ófeigsson et al. (2011) analyzed InSAR data during 1993–2008 to estimate an average location of inflation and deflation (63.9880°N, 19.6434°W), assuming a spherical source. A study by Geirsson et al. (2012) investigated several different source types (spherical, ellipsodial, and pipe) for an inflating source beneath Hekla finding optimal locations, source depths, and volume changes using GPS data from a denser network in the Hekla/Torfajökull area, spanning 2000–2010. They concluded that the optimal source was either an ellipsoid or a sphere, located near the summit of Hekla (see Figure 12).

Next, we use the areal strain rates to find the source depth and volume change for each time interval, assuming a Mogi source at the fixed average location. This is done by first plotting the areal strain rates along many E-W profiles at different latitudes, across the Hekla area (Figure 13). The curves to the west of Hekla are fairly consistent along profiles both to the north and south of Hekla, where we have a relatively dense GPS network. The present study does not, however, include many GPS stations east of Hekla, so the areal strain rates have more scatter toward the east. Also, one should bear in mind that the location of the maximum areal strain can depend on the network geometry, which varies with time. In addition, we suspect that signals due to subsidence at Torfajökull (Geirsson et al., 2012; Scheiber-Enslin et al., 2011) and inflation/deflation due to the Eyjafjallajökull eruption in 2010 affect the strain rates east of Hekla. We therefore only consider the parts of the profiles west of Hekla for our analysis.

Table 1
Depth and Volume Increase for a Mogi Source Under Hekla[a]

Year	Depth (z) (km)	ΔV (km^3/year)	Background (10^{-8}/year)	RMS (10^{-8}/year)
2001–2003	18.7	0.017	4.1	3.5
2003–2005	27.1	0.036	−6.3	1.7
2005–2007	28.7	0.049	−10.1	4.8
2007–2008	19.6	0.018	−4.8	6.2
2008–2009	22.3	0.027	−4.7	3.9
2009–2011	27.0	0.049	−13.2	7.9
2011–2013	20.5	0.025	0.6	10.2
2013–2015	29.4	0.085	−19.4	6.1
2001–2003	20.98	0.024	1.5	3.3
2003–2005	20.98	0.016	−0.1	2.9
2005–2007	20.98	0.018	−1.3	5.9
2007–2008	20.98	0.022	−6.4	5.8
2008–2009	20.98	0.022	−3.0	4.0
2009–2011	20.98	0.021	−4.1	9.5
2011–2013	20.98	0.027	−0.1	10.1
2013–2015	20.98	0.027	−3.6	8.8

[a]Source parameters, background areal strain rate, and root-mean-square (RMS).

The inversion for the depth and volume change is performed in two stages. The main stage obtains the source depth and the Mogi source volume change (ΔV) by fitting the longitudinal derivative of the areal strain rate (i.e., effectively a VDoHS rate term) to the Mogi model prediction, using a weighting proportional to the horizontal distance from the source, and we account for the latitude offsets from each profile through the source. The second stage involves determining a uniform regional/base level adjustment to the predicted areal strain rates to best match the observed areal strain rates. This adjustment is equivalent to estimating small uniform background strain rate for each time interval, as well as strain due to the Mogi source. Estimating a background strain rate is not unreasonable since Hekla is within the deformation zones of the SISZ and EVZ, and the rates we estimate are small (less than 0.1 microstrain per year) considering areal strain rate standard errors. The results are shown in Figure 13 and Table 1. Fitting each time interval separately gives a range of source depths from 18 to 29 km, whereas estimating a constant source depth for all the time intervals gives an optimal source depth of 21 km. The fit to the profiles (depth and volume rate) after 2009 is much worse than for the other time intervals (see Table 1). The volume change of the Mogi source trades off with the source depth; hence, a shallower depth (18.7 km) gives a smaller volume change (0.017 km^3/year) for 2001–2003 than a 21-km depth and a volume change of 0.024 km^3/year (see Table 1). For a fixed source depth of 21 km, the estimated volume change is, however, relatively constant in time ($\sim$0.016–0.022 km^3/year) except for 2011–2013 and 2013–2015, where it appears to be larger (0.027 km^3/year). As noted above, the estimates of magma accumulation after 2009 are less reliable, probably due to the 2010 Eyjafjallajökull eruption.

The constant depth estimate (21 km) is similar to estimates from previous studies for the time interval 2000–2010, that is, an inflating spherical or ellipsoidal source at 24^{+4}_{-2} km using GPS data spanning 2000–2010 by Geirsson et al. (2012) and 17 ± 3-km depth from an InSAR study by Ófeigsson et al. (2011) during 2003–2008. The variation in source depth that we find with time could, however, indicate multiple magma sources below Hekla and/or effects of other sources of areal strain, for example, due to the June 2000 earthquakes for the first time interval (2001–2003) and the 2010 Eyjafjallajökull eruption during 2009–2011. The estimated volume increase during 2000–2010 by Geirsson et al. (2012) at a rate of 0.017–0.02 km^3/year agrees with our estimates during the same period. A lower rate of 0.005±0.002 km^3/year was estimated during 2003–2008 from the InSAR study by Ófeigsson et al. (2011).

The total volume increase (magma accumulation) during 2001–2009 inferred from our study is about 0.16 km^3 and 0.15 km^3 during 2009–2015, bringing the total volume increase for the 15-year time interval to 0.31 km^3, assuming a constant source depth of 21 km. The four previous eruptions at Hekla were every 10 years (in

1970, 1980–1981, 1991, and 2000). The next eruption was therefore expected in 2010 but has not occurred yet at the time of this writing (May 2018). The Eyjafjallajökull eruption in 2010 caused observable deformation and strain changes over a large area and could therefore have affected the magma system beneath Hekla. Our estimates of the magma accumulation at Hekla indicate that the volume of the next eruption is likely to be larger than the four previous eruptions, each of which generated 0.15–0.2 km^3 of eruptive material (dense rock equivalent; Höskuldsson et al., 2007).

6. Discussion

6.1. Postseismic Transients

Two pairs of moderate size main shocks ruptured N-S right-lateral strike-slip faults in the SISZ early in the 21st century. The first pair of main shocks struck the eastern and central part of the zone with two M6.5 events, on 17 and 21 June 2000 (Árnadóttir et al., 2001; Pedersen et al., 2003). A second doublet occurred on 29 May 2008, with two M6 events occurring within a few seconds of each other (Decriem et al., 2010; Hreinsdóttir et al., 2009). Coulomb failure stress calculations indicate that static stress changes due to the June 2000 main shocks loaded the faults that ruptured in the May 2008 main shocks (Árnadóttir et al., 2003).

It is interesting to compare the postseismic transients observed at GPS stations following these two pairs of main shocks. The GPS station velocities during 2001–2003 indicate rather small velocity changes in the epicentral area of the June 2000 main shocks (Figure 4a), with northward motion at stations NW of the main shocks, and more southward motion at stations in the SE quadrants, than in the subsequent time intervals. This is also reflected in higher shear strain (1 microstrain per year) in the epicentral area of the June 2000 main shocks during 2001–2003 but deceasing to ∼0.5 microstrain per year in the subsequent time intervals (Figure 7). Note, however, that the first time interval (2001–2003) does not include the first year of postseismic deformation following the June 2000 main shocks (i.e., 2000–2001). In comparison, the velocity changes following the two M6 main shocks on 29 May 2008 appear to be larger and last longer than for the June 2000 events. In addition, the postseismic transient after 2008 is more pronounced in the area west of the epicentral area. This is evident both from the continuous GPS station time series (Figures 2 and 3) and GPS campaign station velocities after mid-2008 (Figure 4b). The shear strain rates in the epicentral area of the May 2008 main shock are very large (up to 6 microstrains per year) during 2008–2009 and remain quite high (larger than 1 microstrain per year) for the rest of the time interval 2009–2015 (Figure 7). Afterslip during the first year after the 2008 main shocks, on the faults that ruptured, is indicated in the time series at the CGPS stations in the epicentral area (see, e.g., HVER in Figure 2 and SELF in Figure 3).

The large velocity changes and long duration of the transient to the west of the May 2008 epicenters may indicate lateral variation in crustal thickness and possibly lower viscosity in the volcanic area of Hengill than further east in the SISZ. The increase in extraction of geothermal fluids after 2006 in Hengill does, however, enhance the contraction in the Hengill area, influencing the pattern of deformation immediately west of the May 2008 epicentral area. The effect of the Hengill contraction, as well as the background plate motion, needs to be taken into account before a meaningful interpretation of the postseismic deformation is attempted. Modeling of the 2008 postseismic transient is, however, outside the scope of this study.

6.2. Strain in Eastern and Western SISZ

Based on the previous earthquake sequence (1896–1912), one possible location of the next M6–7 event is in the eastern part of the SISZ, east of the 17 June 2000 main shock (Figure 1). In 2013 and 2014 there were swarms of microseismicity on faults in the eastern part of the SISZ (near 20.2°W and 20°W; see Figure S8). The western cluster is near a fault that probably ruptured in an earthquake in 1630 (Einarsson, 2008). Both areas have higher shear strain rates (∼0.7–1 microstrain per year) after 2009 than during 2001–2008 (Figure 7).

Other possible areas of M6 main shock(s) are to the west of Hengill, in the Geitafell and Bláfjöll area, near and west of the continuous GPS station GFEL (Figure 1). There, large strike-slip faults have been mapped, and the shear strain appears to be elevated (>0.7 microstrain per year) during most of the time interval after mid-2008–2015 (Figure 7). Several swarms of microearthquakes, with events reaching M4.2, occurred there in 2012 (see Figure S7). These areas are therefore worth monitoring closely both for deformation and microseismicity.

6.3. Comparison With Other VDoHS Studies

The velocities predicted from the inversion (VDoHS rates) and the observed GPS velocities are shown in the supporting information (Figures S1–S8). For the most part, the predicted velocities (black arrows) are identical

to the observations (colored arrows). This indicates that the VDoHS method is able to fit the data well and generate a robust estimate of the strain rates.

The VDoHS method allows us to estimate both spatial and temporal variation in areal and shear stress in South Iceland. The strain rates in the SISZ are very large compared to previous studies using VDoHS in New Zealand (Dimitrova et al., 2016). The New Zealand study indicates areal strain rates ranging from -0.1 to 0.1 microstrain per year and maximum shear strain rates of up to 0.3 microstrain per year along the prominent strike-slip faults in the northern part of the South Island. The spreading rate across Iceland (18–19 mm/year) is smaller than the the convergence rate in New Zealand (27–57 mm/year), from south to north along the Hikurangi margin (Dimitrova et al., 2016). When a concentrated source in an elastic medium is at a depth z, the zone at the surface where clearly noticeable strains are observed will be at least $2z$ wide — that is, from $x - z$ to $x + z$, where x is the horizontal position of the source. Therefore, for a source at a depth of 50 km, for example, the zone of observed straining will be of order 100 km wide. Hence, the high, concentrated strain rates in Iceland indicate that the sources are shallow. The zone of elastic deformation is only ∼20 km wide, and it is difficult to accommodate sources deeper than 10 km in such a narrow zone. The shallow sources and multiple processes in the SISZ make it difficult to interpret the rather complex pattern of the VDoHS rate vectors.

7. Conclusions

We calculate GPS station velocities in South Iceland during 2001–2015 and find significant velocity changes both temporally and spatially. We estimate strain rates from the GPS velocities, using two methods: a well-established method (Beavan & Haines, 2001; Haines & Holt, 1993) and a new method that uses the VDoHS (Haines et al., 2015). Both methods indicate similar patterns and magnitudes of the shear and areal strain rates.

Areal strain rates indicate contraction in the Hengill area, consistent with subsidence due to geothermal fluid extraction at two power plants and a deep source of contraction in the area (Juncu et al., 2017). We also find a wide area of extension around Hekla volcano, indicating magma accumulation beneath the volcano since the last eruption in February 2000. We use strain rates around Hekla to estimate an average location of an inflating Mogi source and then find depths and volume changes for each time interval. The source depths do not appear to vary systematically with time, and the signal can be fit with a constant depth of ∼21 km, as there is trade-off between depth and volume change. Assuming a single Mogi source depth of ∼21 km, we estimate an average rate of volume increase of ∼0.02 km^3/year for the 2001–2015 time interval.

We find high shear strain rates in the SISZ, in particular, following the May 2008 main shocks. The strain anomaly we observe prior to the May 2008 main shocks is primarily due to plate motion and contraction in Hengill area, which causes elevated shear strain rates, and dilatation, possibly decreasing the normal stress on N-S oriented faults in Ölfus. It is noteworthy that the postseismic shear strain rates appear higher in the May 2008 epicentral area than what we observe following the June 2000 main shocks, although the latter were larger events. The strain rate remains high still in the Ölfus and Hengill areas during 2013–2015. During 2008–2015 we observe high shear strain rates in the eastern part of the SISZ, and west of Hengill, that may indicate a buildup toward future $M6$–7 main shock(s).

References

Altamimi, Z., Métivier, L., & Collilieux, X. (2012). ITRF2008: Plate motion model. *Journal of Geophysical Research*, *117*, B07402. https://doi.org/10.1029/2011JB008930

Antonioli, A., Belardinelli, M., Bizzarri, A., & Vogfjörd, K. S. (2006). Evidence of instantaneous dynamic triggering during the seismic sequence of year 2000 in South Iceland. *Journal of Geophysical Research*, *111*, B03302. https://doi.org/10.1029/2005JB003935

Argyris, J., Fried, I., & Scharpf, D. (1968). The TUBA family of plate elements for the matrix displacement method, aeronaut. *Journal of the Royal Aeronautical Society*, *72*, 701–709.

Árnadóttir, T., Hreinsdóttir, S., Gudmundsson, G., Einarsson, P., Heinert, M., & Völksen, C. (2001). Crustal deformation measured by GPS in the South Iceland Seismic Zone due to two large earthquakes in June 2000. *Geophysical Research Letters*, *28*, 4031–4033.

Árnadóttir, T., Jiang, W., Feigl, K. L., Geirsson, H., & Sturkell, E. (2006). Kinematic models of plate boundary deformation in southwest Iceland derived from GPS observations. *Journal of Geophysical Research*, *111*, B07402. https://doi.org/10.1029/2005JB003907

Árnadóttir, T., Jónsson, S., Pedersen, R., & Gudmundsson, G. B. (2003). Coulomb stress changes in the South Iceland Seismic Zone due to two large earthquakes in June 2000. *Geophysical Research Letters*, *30*(5), 1205. https://doi.org/10.1029/2002GL016495

Árnadóttir, T., Jónsson, S., Pollitz, F. F., Jiang, W., & Feigl, K. L. (2005). Postseismic deformation following the June 2000 earthquake sequence in the South Iceland Seismic Zone. *Journal of Geophysical Research*, *110*, B12308. https://doi.org/10.1029/2005JB003701

Árnadóttir, T., Lund, B., Jiang, W., Geirsson, H., Björnsson, H., Einarsson, P., & Sigurdsson, T. (2009). Glacial rebound and plate spreading: Results from the first countrywide GPS observations in Iceland. *Geophysical Journal International*, *177*(2), 691–716. https://doi.org/10.1111/j.1365-246X.2008.04059.x

Beavan, J., & Haines, J. (2001). Contemporary horizontal velocity and strain rate fields of the Pacific-Australian plate boundary zone through New Zealand. *Journal of Geophysical Research*, *106*, 741–770.

Bjarnason, I., Cowie, P., Anders, M. H., Seeber, L., & Scholz, C. H. (1993). The 1912 Iceland earthquake rupture: Growth and development of a nascent transform system. *Bulletin of the Seismological Society of America*, *83*, 416–435.

Clifton, A. E., & Kattenhorn, S. (2006). Structural architecture of a highly oblique divergent plate boundary segment. *Tectonophysics*, *419*, 27–40.

Decriem, J., & Árnadóttir, T. (2012). Transient crustal deformation in the South Iceland Seismic Zone observed by GPS and InSAR during 2000–2008. *Tectonophysics*, *581*, 6–18. https://doi.org/10.1016/j.tecto.2011.09.028

Decriem, J., Árnadóttir, T., Hooper, A., Geirsson, H., Sigmundsson, F., Keiding, M., et al. (2010). The 29 May 2008 earthquake doublet in SW Iceland. *Geophysical Journal International*, *181*, 1128–1146. https://doi.org/10.1111/j.1365-246X.2010.04565.x

DeMets, C. G., Gordon, R., & Argus, D. F. (2010). Geologically current plate motions. *Geophysical Journal International*, *181*, 1–80. https://doi.org/10.1111/j.1365-246X.2009.04491.x

Dimitrova, L. L., Wallace, L. M., Haines, A. J., & Williams, C. A. (2016). High-resolution view of active tectonic deformation along the Hikurangi subduction margin and the Taupo Volcanic Zone, New Zealand. *New Zealand Journal of Geology and Geophysics*, *59*, 43–57. https://doi.org/10.1080/00288306.2015.1127823

Einarsson, P. (2008). Plate boundaries, rifts and transforms in Iceland. *Jökull*, *58*, 35–38.

Einarsson, P., Björnsson, S., Foulger, G., Stefánsson, R., & Skaftadóttir, T. (1981). Seismicity pattern in the South Iceland Seismic Zone. In D. W. Simpson & P. G. Richards (Eds.), *Earthquake prediction—An international review* (Vol. 4, pp. 141–151). Washington, DC: American Geophysical Union.

Einarsson, P., Sigmundsson, F., Sturkell, E., Árnadóttir, T., Pedersen, R., Pagli, C., & Geirsson, H. (2006). Geodynamic signals detected by geodetic methods in Iceland. In C. Hirt (Ed.), *Festschrift for Prof. G. Seeber* (pp. 39–57). Hannover, Germany: Wissenschaftliche Arbeiten der Fachrichtung Geodäsie und Geoinformatik der Universität Hannover Nr. 258.

Feigl, K. L., Gasperi, J., Sigmundsson, F., & Rigo, A. (2000). Crustal deformation near Hengill Volcano, Iceland 1993–1998: Coupling between magmatic activity and faulting inferred from elastic modeling of satellite radar interferograms. *Journal of Geophysical Research*, *105*, 25,655–25,670.

Geirsson, H., Árnadóttir, T., Hreinsdóttir, S., Decriem, J., LaFemina, P. C., Jónsson, S., et al. (2010). Overview of results from continuous GPS observations in Iceland from 1995 to 2010. *Jökull*, *60*, 3–22. https://doi.org/10.1029/2012JB009400

Geirsson, H., LaFemina, P. C., Árnadóttir, T., Sturkell, E., Sigmundsson, F., Schmidt, P., et al. (2012). Volcano deformation at active plate boundaries: Deep magma accumulation at Hekla volcano and plate boundary deformation in South Iceland. *Journal of Geophysical Research*, *117*, B11409. https://doi.org/10.1029/2012JB009400

Haines, A. J., Dimitrova, L. L., Wallace, L. M., & Williams, C. A. (2015). *Enhanced surface imaging of crustal deformation: Obtaining tectonic force fields using GPS data* (pp. 99). Germany: Springer. https://doi.org/10.1007/978-3-319-21578-5

Haines, A. J., & Holt, W. E. (1993). A procedure for obtaining the complete horizontal motions within zones of distributed deformation from the inversion of strain rate data. *Journal of Geophysical Research*, *98*, 12,057–12,082.

Herring, T. A., King, R. W., Floyd, M. A., & McClusky, S. C. (2015). Introduction to GAMIT/GLOBK, Release 10.6. MA, USA: Mass. Inst. Technol.

Höskuldsson, A., Óskarsson, N., Pedersen, R., Grönvold, K., Vogfjörd, K., & Ólafsdóttir, R. (2007). The millennium eruption of Hekla in February 2000. *Bulletin of Volcanology*, *70*, 169–182.

Hreinsdóttir, S., Árnadóttir, T., Decriem, J., Geirsson, H., Tryggvason, A., Bennett, R. A., & LaFemina, P. (2009). A complex earthquake sequence captured by the continuous GPS network in SW Iceland. *Geophysical Research Letters*, *36*, L12309. https://doi.org/10.1029/2009GL038391

Jakobsdóttir, S. S. (2008). Seismicity in Iceland. *Jökull*, *58*, 75–100.

Jaynes, E. (1957a). Information theory and statistical mechanics. *Physical Review*, *106*, 620–630. https://doi.org/10.1103/PhysRev.106.620

Jaynes, E. T. (1957b). Information theory and statistical mechanics. II. *Physical Review*, *108*, 171–190. https://doi.org/10.1103/PhysRev.108.171

Jaynes, E. T. (1968). Prior probabilities. *IEEE Xplore: IEEE Transactions on Systems Science and Cybernetics*, *4*, 227–241. https://doi.org/10.1109/TSSC.1968.300117

Jaynes, E. (1988). The relation of Bayesian and maximum entropy methods. In G. Erickson & C. Smith (Eds.), *Maximum-entropy and Bayesian methods in science and engineering* (Vol. 31–32, pp. 25–29). Dordrecht, Netherlands: Springer.

Jónsson, S. (2008). Importance of post-seismic viscous relaxation in southern Iceland. *Nature Geoscience*, *1*, 136–139. https://doi.org/10.1038/ngeo105

Juncu, D., Árnadóttir, T., Hooper, A., & Gunarsson, G. (2017). Anthropogenic and natural ground deformation in the Hengill geothermal area, Iceland. *Journal of Geophysical Research: Solid Earth*, *122*, 692–709. https://doi.org/10.1002/2016JB013626

Keiding, M., Árnadóttir, T., Sturkell, E., Geirsson, H., & Lund, B. (2008). Strain accumulation along an oblique plate boundary: The Reykjanes Peninsula, southwest Iceland. *Geophysical Journal International*, *172*(1), 861–872. https://doi.org/10.1111/j.1365-246X.2007.03655.x

Kreemer, C., Blewitt, G., & Klein, E. C. (2014). A geodetic plate motion and global strain rate model. *Geochemistry, Geophysics, Geosystems*, *15*, 3849–3889. https://doi.org/10.1002/2014GC005407

Kreemer, C., Holt, W., & Haines, A. J. (2003). An integrated global model of present-day plate motions and plate boundary deformation. *Geophysical Journal International*, *154*, 8–34.

Linde, A. T., Ágústsson, K., Sacks, I., & Stefánsson, R. (1993). Mechanism of the 1991 eruption of Hekla from continuous borehole strain monitoring. *Nature*, *365*, 737–740.

Lyard, F., Lefevre, F., Letellier, T., & Francis, O. (2006). Modelling the global ocean tides: Modern insights from FES2004. *Ocean Dynamics*, *56*(5–6), 394–415. https://doi.org/10.1007/s10236-006-0086-x

Mogi, K. (1958). Relations between the eruptions of various volcanoes and the deformation of the ground surfaces around them. *Bulletin of the Earthquake Research Institute*, *36*, 99–134.

Ófeigsson, B. G., Hooper, A., Sigmundsson, F., Sturkell, E., & Grapenthin, R. (2011). Deep magma storage at Hekla volcano, Iceland, revealed by InSAR time series analysis. *Journal of Geophysical Research*, *116*, B05401. https://doi.org/10.1029/2010JB007576

Pedersen, R., Jónsson, S., Árnadóttir, T., Sigmundsson, F., & Feigl, K. L. (2003). Fault slip distribution of two M_w =6.5 earthquakes in South Iceland estimated from joint inversion of InSAR and GPS measurements. *Earth and Planetary Science Letters*, *213*, 487–502.

Ruppert, J. (1995). A Delaunay refinement algorithm for quality 2-dimensional mesh generation. *Journal of Algorithms*, *18*, 548–585. https://doi.org/10.1006/jagm.1995.1021

Sandwell, D., & Wessel, P. (2016). Interpolation of 2-D vector data using constraints from elasticity. *Geophysical Research Letters*, *43*, 10,703–10,709. https://doi.org/10.1002/2016GL070340

Scheiber-Enslin, S. E., LaFemina, P. C., Sturkell, E., Hooper, A. J., & Webb, S. J. (2011). Geodetic investigation of plate spreading along a propagating ridge: The Eastern Volcanic Zone, Iceland. *Geophysical Journal International*, *187*(3), 1175–1194. https://doi.org/https://doi.org/10.1111/j.1365-246X.2011.05243.x

Segall, P. (2016). Repressurization following eruption from a magma chamber with a viscoelastic aureole. *Journal of Geophysical Research: Solid Earth*, *121*, 8501–8522. https://doi.org/10.1002/2016JB013597

Sigmundsson, F., Einarsson, P., & Bilham, R. (1992). Magma chamber deflation recorded by the global positioning system: The Hekla 1991 eruption. *Geophysical Research Letters*, *19*(14), 1483–1486. https://doi.org/10.1029/92GL01636

Sigmundsson, F., Einarsson, P., Rögnvaldsson, S. T., Foulger, G. R., Hodgkinsson, K. M., & Thorbergsson, G. (1997). The 1994–1995 seismicity and deformation at the Hengill triple junction, Iceland: Triggering of earthquakes by minor magma injection in a zone of horizontal shear stress. *Journal of Geophysical Research*, *102*(B7), 15,151–15,161.

Sigmundsson, F., Hreinsdóttir, S., Hooper, A., Árnadóttir, T., Pedersen, R., Roberts, M. J., et al. (2010). Intrusion triggering of the 2010 Eyjafjallajökull explosive eruption. *Nature*, *468*, 426–430. https://doi.org/10.1038/nature09558

Sturkell, E., Ágústsson, K., Linde, A. T., Sacks, S. I., Einarsson, P., Sigmundsson, F., et al. (2013). New insights into volcanic activity from strain and other deformation data for the Hekla 2000 eruption. *Journal of Volcanology and Geothermal Research*, *256*, 78–86. https://doi.org/10.1016/j.jvolgeores.2013.02.001

Sturkell, E., Einarsson, P., Sigmundsson, F., Geirsson, H., Ólafsson, H., Pedersen, R., et al. (2006). Volcano geodesy and magma dynamics in Iceland. *Journal of Volcanology and Geothermal Research*, *150*, 14–34. https://doi.org/10.1016/j.jvolgeores.2005.07.010

Tarantola, A. (1987). *Inverse problem theory*. Amsterdam: Elsevier.

Tarantola, A., & Valette, B. (1982). Inverse problems—Quest for information. *Journal of Geophysics*, *50*, 159–170.

Thordarson, T., & Larsen, G. (2007). Volcanism in Iceland in historical time: Volcano types, eruption styles and eruptive history. *Journal of Geodynamics*, *43*, 118–152.

Wessel, P., Smith, W. H. F., Scharroo, R., Luis, J. F., & Wobbe, F. (2013). Generic Mapping Tools: Improved version released. *Eos, Transactions American Geophysical Union*, *94*, 409–410.